Rotational damping, ridges, and the quasicontinuum of γ rays in ^{152}Dy

T. Lauritsen, R. V. F. Janssens, T. L. Khoo, I. Ahmad, M. P. Carpenter, F. G. Kondev,
C. J. Lister, E. F. Moore, D. Seweryniak, and S. Zhu

Argonne National Laboratory, Argonne, Illinois 60439, USA

T. Døssing and B. Herskind

Niels Bohr Institute, DK-2100, Copenhagen, Denmark

A. Korichi and A. Lopez-Martens

C.S.N.S.M, IN2P3-CNRS, bat 104-108, F-91405 Orsay Campus, France

R. M. Clark, P. Fallon, G. Lane, A. O. Macchiavelli, and D. Ward

Lawrence Berkeley National Laboratory, Berkeley, California 94720, USA

A. M. Heinz

A. W. Wright Nuclear Structure Laboratory, Yale University, New Haven, Connecticut 06520, USA

D. G. Jenkins

Department of Physics, University of York, Heslington, York YO10 5DD, United Kingdom

A. J. Larabee, B. Meredith, and J. Kozemczak

Greenville College, Greenville, Illinois 62246, USA

P. Chowdhury

University of Massachusetts, Lowell, Massachusetts 01854, USA

The quasicontinuum of γ rays from the feeding and decay of superdeformed and normal bands in ^{152}Dy have been extracted in one- and two-dimensional spectra. The E_γ-E_γ correlations in the latter reveal strong ridges associated with superdeformed and normal states in this nucleus. The entry distributions for normal and superdeformed bands have been extracted from measured fold and sum-energy distributions. A Monte Carlo model was developed to *simultaneously* describe all the quasicontinuum and ridge spectra as well as the feeding intensity of the superdeformed bands. The rotational damping widths in the normal and superdeformed wells were derived based on a comparison of the data with model calculations of the continuum of γ rays at finite temperature.

I. INTRODUCTION

In several regions of the chart of nuclei, shell effects lead to the presence of an excited minimum in the total energy surface associated with a large prolate deformation. The major to minor axis ratio may be as as large as $\sim$2:1 in this minimum [1,2]. The properties of the excitations occurring in this superdeformed (SD) minimum continue to be a subject of much interest. Superdeformation in ^{152}Dy was originally discovered by studying correlated ridges, i.e., structures parallel to the diagonal in γ-γ coincidence matrices [3,4]. Only afterward was the first discrete SD band discovered [5]. It took as many as 16 years to find the links of this SD band to the normal deformed (ND) states it decays into [6], and recently the excited SD band 6, built on an octupole vibration, was linked to the yrast SD band as well [7]. These two discoveries were only possible because a very large data set was collected with Gammasphere (GS) [8]. This data set

also makes it possible to take a new look at the continuum of γ rays with much higher precision than was the case earlier [3,4].

After the last particle has been evaporated, the cooling of a nucleus, formed in a heavy-ion fusion evaporation reaction, is by emission of γ rays (or converted γ rays, at low energy). At finite temperature above the yrast line, the level density is high and the γ rays form a quasicontinuum (QC) spectrum from which individual γ rays cannot be resolved. Only when the γ cascades reach states on or near the yrast line are discrete transitions observed. The QC spectra from the hot region above the yrast line contain not only information about the feeding mechanism of ND and SD discrete bands and the properties of states at finite temperature [9–13], but also, in the case of SD bands, information about the decay of the SD bands into ND levels. The latter QC decay spectrum has been used to determine the spin and excitation energy of SD bands when discrete linking transitions could not be found [9,10]. It is

the aim of this paper to fully delineate the QC spectra from the feeding of ND and SD bands as well as the QC spectrum associated with the decay of SD band 1 in ^{152}Dy.

Correlations in γ-γ coincidence matrices allow for a determination of the important rotational damping [14–31] at finite temperature. In a region where the level density is high, $E2$ transitions are no longer just simple intraband transitions, because the level spacing is smaller than or comparable to the matrix elements of the residual interaction (i.e., two or more body interactions beyond the mean field treatment) [32,33]. The initial and final states are complicated superpositions resulting from the mixing of a large number of levels. The ensuing distribution of γ-ray energies out of each such state acquires a width, the rotational damping width, the half width at half maximum (HWHM) of which is denoted by $\Gamma_{\rm rot}^{(2)}$ [23,25]. In addition, γ-γ correlation matrices also contain information about more specific two-step correlations, described by a more narrow width, Γ_μ [19,24,29–31]. This quantity is often referred to as $\Gamma_{\rm comp}$, the compound damping width [34]. The connection between the compound damping width and the narrow rotational damping width was established by Matsuo *et al.* [24].

To gain more insight into the physical significance of the wide ($\Gamma_{\rm rot}^{(2)}$) and narrow (Γ_μ) rotational damping parameters, it may be instructive to consider them in the time domain as suggested by Døssing *et al.* [20]. The narrow rotational damping width Γ_μ describes the spread of simple states, e.g., levels described in a shell model, over the nuclear compound states which include residual interactions. It follows that $\hbar/\Gamma_\mu$ describes the average time the nucleus spends in the simple shell model states. On the other hand, $\hbar/\Gamma_{\rm rot}^{(2)}$ describes the average time it takes for the compound state that originated at spin I to spread into the compound states at spin I-2 through the $E2$ decay [20,35]. In this time domain, it is easy to understand the effect of motional narrowing, i.e., the effect that the wide component starts to decrease at higher excitation energies after initially increasing as a function of excitation energy. At some finite excitation energy, Γ_μ becomes large enough, and thus $\hbar/\Gamma_\mu$ small enough, that the nucleus does not spend sufficient time in a particular shell model state to have time to spread over the states at spin I-2 before it "jumps" to another shell model state. Thus, the effective width of the rotational damping $\Gamma_{\rm rot}^{(2)}$ will start to decrease again with increasing excitation energy in analogy with the similar well-known effects in nuclear magnetic resonances [16,20] and the damping of giant resonances in hot nuclei [36].

The compound damping width $\Gamma_{\rm comp}$ increases monotonically with the excitation energy above the yrast line (also known as heat energy or the intrinsic excitation energy), U [15]. On the other hand, the wide rotational damping width $\Gamma_{\rm rot}^{(2)}$ is expected to reach a maximum and then decrease again as discussed above (see, e.g., Refs. [15,16,20,34]). When the estimated $\Gamma_{\rm comp}$ is smaller than the spacing D_2 of levels, which can interact via a two-body interaction, discrete bands of specific structure will be seen. This is generally the case at the lowest excitation energies above yrast, typically below $U < 1$ MeV. Above this energy, band mixing sets in, and this generally leads to damping of the rotational motion with $E2$

transitions spreading out of each state to many final levels. Still higher up in heat energy, the compound damping width dominates, and the motional narrowing discussed above occurs [15,34]. Under very special circumstances, the band mixing at neighboring angular momenta may be correlated, producing rotational bands with strong $E2$ transitions, based on mixed states with many components. Such bands, referred to as ergodic bands [32,37], requires either very large deformations or special shell structure for the intrinsic states; this is not expected to occur for ^{152}Dy but has been observed for excited SD states in ^{194}Hg [38]. However, the regions of rotational damping and motional narrowing are both expected to be probed by the γ cascades that cool the nucleus and feed the ND and SD discrete levels.

Under the condition $\Gamma_\mu > \Gamma_{\rm rot}^{(2)} > D$, when U is of the order of 8 MeV, the distribution of excited levels is expected to be chaotic and can be described by a full Gaussian orthogonal ensemble (GOE) distribution [14,32,39]. At lower excitation energies, sparse GOE distributions might provide a better description [39]. However, in the treatment described below, only the full GOE description, implying chaos [40], is used. In fact, it should be possible to relate the strength of rotational damping to chaos in nuclei at finite temperature [20,41].

Besides investigating the one-dimensional (1D) ND and SD QC spectra and two-dimensional (2D) ridges, the main aim of this work was to extract the rotational damping parameters $\Gamma_{\rm rot}^{(2)}$, Γ_μ and the relative intensities of the narrow damping component, $I_{\rm nar}$, for ^{152}Dy. The general outline of this paper is as follows. First, the QC spectra and ridges in coincidence with ND and SD discrete γ rays in ^{152}Dy are presented. This is followed by a discussion of results of a dedicated experiment in which the (total) entry distribution was measured with GS. The extraction of the entry distribution will also make use of the results of a decomposition of the QC spectra, where coincidence gates are placed on discrete ND transitions. The measured entry distribution will subsequently be the starting point for γ cascades that are followed in Monte Carlo (MC) simulations, in an attempt to *simultaneously* reproduce the ND and SD QC and ridge spectra. The reproduction of these spectra allows the determination of the rotational damping strengths in the SD and ND wells of ^{152}Dy. Furthermore, the simulations also elucidate the mechanisms associated with feeding and decay of SD bands in the $A \sim 150$ mass region. For simplicity, first fixed (average) values of $\Gamma_{\rm rot}^{(2)}$, Γ_μ, and $I_{\rm nar}$ will be used in the MC calculations (referred to as MC1 calculations). Then, simulations of these quantities incorporating more realistic variations with spin and excitation energy (referred to as MC2 calculations) will be discussed. Finally, the SD entry distribution will be extracted and compared with the total entry distribution for ^{152}Dy.

II. EXPERIMENT DETAILS

The ND and SD bands in ^{152}Dy were populated with the reaction ^{108}Pd(^{48}Ca,$4n$)^{152}Dy at 191 MeV (midtarget). In the first experiment, the ^{48}Ca beam was delivered by the 88-in. cyclotron facility at the Lawrence Berkeley National Laboratory, and the target consisted of a stack of two $\sim$0.4 mg/cm^2

self-supporting ^{108}Pd foils. The γ rays were measured with the GS array [8], comprised of 100 Compton suppressed Ge detectors. As described in Ref. [6], events associated with the ^{152}Dy reaction channel were selected (tagged) by detecting the decay of the 86-ns, 17$^+$ yrast isomer [42,43] on a Pb stopper foil placed about 30 cm downstream from the target, amid the most forward BGO detectors [44] of the GS array. The beam drilled a hole in the stopper foil while most of the residues of interest were deposited on the foil because of small angle scattering. The tagging efficiency was measured to be ∼80%. A total of 1.6×10^9 ^{152}Dy events were isomer tagged during a 12-day run.

In the second, shorter follow-up experiment, the Hevimet shields, an alloy of tungsten, were removed from the BGO detectors in GS in order to measure the ND and SD entry distributions. This time, the ^{48}Ca beam was delivered by the Argonne Tandem-Linac Accelerator System (ATLAS) at Argonne National Laboratory. The reaction and setup were otherwise identical. This experiment ran for 6 days during which time a total of 4.8×10^8 isomer-tagged events were collected.

In the first experiment, the BGO detectors had the Hevimet shields on, and the Ge crystals had thick 1.27-mm Pb absorbers in front of them to attenuate low-energy γ rays. In the second experiment, the absorbers consisted of 0.05-mm Ta, 0.51-mm Cd and 0.25-mm Cu sheets, while the BGO detectors had 1.27-mm Pb absorbers in front of them to shield against target x rays. In both experiments, the timing discriminators for the Ge detectors were operated in constant-fraction mode with slow-rise-time rejection.

III. DECOMPOSITION OF NORMAL DEFORMED QUASICONTINUUM SPECTRA

Pairs of double coincidence gates were placed on the following ND lines in ^{152}Dy: 1114.5, 779.6, 684.9, 388.6, and 967.0 keV, covering the spin range 28–37$\hbar$ (see Refs. [42,43,45] for a suitable level scheme). The resulting γ rays were sorted "spike free" [46] into 1D spectra associated with the 17 polar angles of GS [8]: 17.27°, 31.72°, 37.38°, 50.07°, 58.28°, 69.82°, 79.19°, 80.71°, 90.00°, 99.29°, 100.81°, 110.18°, 121.78°, 129.93°, 142.62°, 148.28°, and 162.73°. So-called local background spectra, i.e., coincidence spectra with gates placed in the direct vicinity of the lines themselves in the E_γ-E_γ plane, were subtracted for each gate combination and each angle, using the procedure described in Ref. [47]. The statistical errors were carefully propagated. These spectra were then corrected further for a number of effects described below.

First, the contributions due to coincidence summing were removed [48]. The summing factor was estimated as

$$R = 1 - (1 - \Omega)^{M-2}; \quad \Omega \equiv \frac{\epsilon_p}{P_T}, \qquad (1)$$

where ϵ_p is the absolute photopeak [49] efficiency (see Appendix A) at the mean energy of the unfolded spectrum, P_T is the photopeak to total ratio (also at this energy), and M is the multiplicity of the unfolded spectrum described below.

The P_T value is found from the response function, which is described below as well. Since M and the mean energy of the unfolded spectrum have not been determined at this point of the analysis process, estimates are made and the final values are found in an iterative process. A final adjustment of R is made until the summed peaks in the spectrum are reduced as much as possible. A small contribution associated with neutron interactions in the Ge detectors, predominantly seen in detectors located at forward angles, was subtracted next using a measured neutron interaction spectrum. This spectrum was found by placing Hevimet shields in front of the Ge detectors such that they only register γ rays generated by neutrons from a heavy-ion fusion reaction striking the detectors [50].

Even with efficient BGO Compton suppression shields, some Compton events are still present in the spectra and must be subtracted in order to extract the true QC contributions. By recording the spectra from (i) single-line sources and (ii) sources emitting two γ rays in coincidence, all placed at the target position, the response function of GS was measured. For the latter sources, single-line spectra were obtained by applying appropriate coincidence gates. Table I lists the sources used to measure the response of the array; i.e., the total spectrum observed in GS when a γ ray of a given energy was emitted in its center. In all cases, the room background was subtracted before the source data were used to construct the response of GS. By interpolating between the measured response functions at neighboring discrete energies, the Compton contributions over the entire spectrum were deduced and subtracted using the unfolding technique described in Ref. [48]. How well this procedure works is demonstrated in Appendix B. Despite the use of 2D energy-dependent time gates, there was a small reduction in the efficiency at low energy, which was corrected for in the response function. The corrections to the spectra described above are illustrated in Fig. 4 of Ref. [9] in the case of ^{192,194}Hg.

The efficiency of GS was measured using the multiline calibration sources [51] ^{152}Eu, ^{182}Ta, ^{243}Am, and ^{56}Co, with the procedure described in Ref. [48]. The spectrum in each polar

TABLE I. Sources used to determine the response function for GS. Background spectra were measured and subtracted from the single-line source data before the latter were used to calibrate the response function used subsequently to unfold the 1D γ-ray spectra.

Source	E_γ (keV)
^{57}Co	122
^{141}Ce	145
^{113}Sn	392
^{85}Sr	514
^{137}Cs	662
^{54}Mn	835
^{65}Zn	1116
^{111}In	171, 145
^{88}Y	898, 1836
^{60}Co	1173, 1333

angle was corrected for efficiency, before applying corrections for Doppler shifts using the relativistic formula [52]

$$E_{LAB}(\theta) = E_{CM} \times F(\beta, \theta); \quad F(\beta, \theta) \equiv \frac{\sqrt{1 - \beta^2}}{1 - \beta \cos\theta}. \quad (2)$$

Here $\beta \equiv v/c$, v is the velocity of the nucleus at the time of γ emission, E_{CM} the γ-ray energy in the center-of-mass system, and $E_{LAB}(\theta)$ the corresponding γ-ray energy in the laboratory at the polar angle θ. At the same time, the spectra were also corrected for relativistic aberrations [52], i.e., the spectra in the laboratory frame were scaled with $[F(\beta, \theta)]^2$, where the $F(\beta, \theta)$ factor is defined in Eq. (2).

The angle-sorted spectra were then fitted with the function

$$W(\theta) = A_0 + A_2 P_2(\cos\theta) + A_4 P_4(\cos\theta) \quad (3)$$

at each energy channel in order to extract the true intensity (A_0) spectrum presented in Fig. 1. The mean γ-ray energy in Fig. 1 is ~1130(40) keV, and the total multiplicity is 21.3(7), corrected for γ rays missing due to the effect of coincidence gating but not for internal conversion. The latter correction would add to the multiplicity and lower the mean energy slightly.

The discrete lines were then removed (at each angle) in an iterative procedure, which uses the information in the propagated statistical error spectra, and both identified and unassigned γ rays were removed. A new A_0 spectrum was then extracted; it is presented, contracted to 32 keV per channel, in Fig. 2. This figure shows the QC of γ rays (or unresolved γ rays) emitted before the ^{152}Dy nucleus has cooled to the point where only discrete γ rays are emitted from the decay of states located on or near the yrast line [9].

The spectra of Figs. 1 and 2 have also been normalized to the number of γ cascades that produced them. Thus, the area
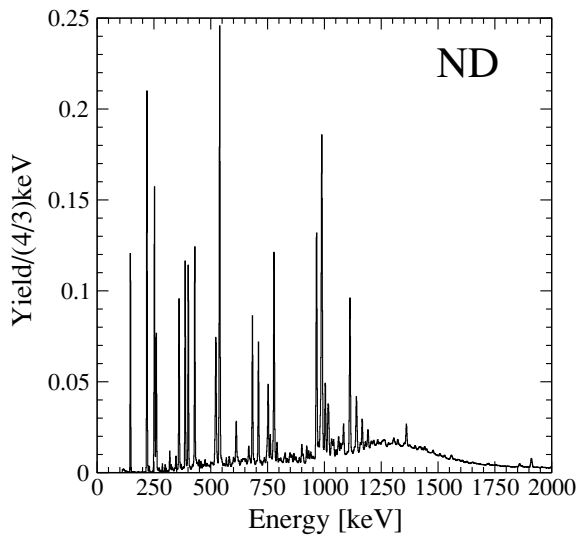

FIG. 1. Sum of angle-sorted spectra after double coincidence gates were placed on ND lines in ^{152}Dy. The data were processed as described in the text and normalized to the number of γ cascades in the data. A distinct continuum, displayed in greater detail in Fig. 2, is clearly visible under the discrete peaks.
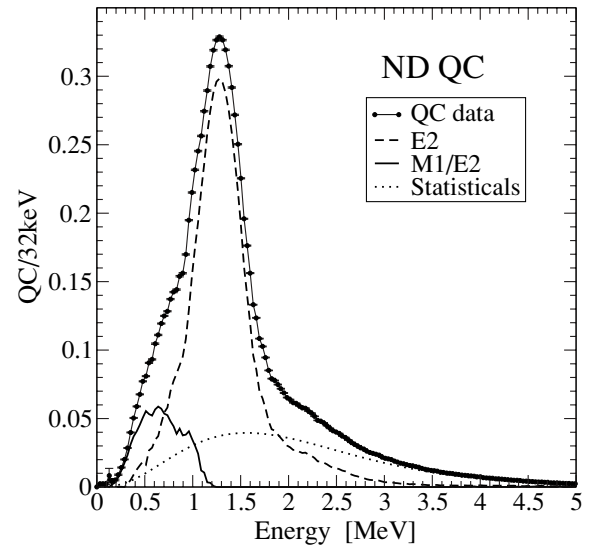

FIG. 2. Same as Fig. 1, but with the discrete peaks removed. The spectrum has been contracted to 32 keV/channel, and the three components of the QC spectrum have been identified through the decomposition procedure described in the text.

of the spectra, or of any parts in them, is equivalent to the associated multiplicity. The 540-keV line ($25^- \rightarrow 23^-$) [43] was used for the normalization. It was found that 76(2)% of the yrast band intensity is contained in the ND 540-keV line, which is not part of any of the double gates used to produce the spectra in Figs. 1 and 2. Thus, the area of this 540-keV transition divided by 0.76(2) was used to normalize the spectra in Figs. 1 and 2 to the number of cascades they represent [9].

As in the $A \sim 190$ mass region [9], the QC spectrum was then decomposed into its different multipole components; i.e., its $E2$ quadrupole, $E1$ statistical, and $M1/E2$ dipole constituents. These three components are presented in Fig. 2 as well. First, the statistical spectrum is fitted to the high-energy part of the QC spectrum with the functional form [50,53–56]

$$f(E) = C E^N e^{-\frac{E}{T}}. \quad (4)$$

A fit was performed from $E = 2.9$–5.1 MeV, and the fit parameters were found to be $C = 3316(34)$, $N = 3.054(8)$, and $T = 0.517(1)$ MeV, where the errors reflect only the statistical uncertainty. The multiplicity and mean energy of the fitted statistical spectrum are given in Table II. After correction for the angular distribution [Eq. (3)] and relativistic aberration [Eq. (2)], this component was then subtracted from the QC spectrum at each polar angle. As a result, only the $E2$ quadrupole and $M1/E2$ dipole components remain, which were further decomposed using the angular distribution analysis carried out using Eq. (3). The resulting A_2/A_0 spectrum is displayed in Fig. 3.

The A_2/A_0 coefficient is sensitive to the multipolarity of the emitted γ rays [57]. Two limits to the value of this coefficient can be specified, as shown in Fig. 3. If the measured A_2/A_0 coefficient at a given energy is at or above the upper limit of $+0.365$, characteristic of stretched $E2$ transitions, then the content of the corresponding A_0 spectrum is considered to

TABLE II. Decomposition of the normalized QC spectrum of Fig. 2 obtained with double coincidence gates placed on ND lines in ^{152}Dy. To arrive at the mean entry point, the contributions from the isomer and from the lines missed because of gating are added. The last row corresponds to the mean spin and energy of the entry distribution measured by the HK method described in Sec. VI. The error estimates contain contributions from statistical uncertainties and systematic errors from the background subtraction, unfolding, and normalization.

Component	Multiplicity M	$\langle E \rangle$ (MeV)	$\delta I/M (\hbar)$	$\Delta I (\hbar)$	ΔE (MeV)
QC:stat	2.9(2)	2.08(2)	0.6(1)[a]	1.7(3)	6.0(3)
QC:$E2$	6.8(4)	1.36(1)	2.0	13.6(7)	9.2(5)
QC:$M1/E2$	1.1(1)	0.75(3)	0.9(1)[a]	1.0(1)	0.9(1)
a/14 ns	6.4(3)			9.0(6)	4.2(3)
b/14 ns	0.9(1)			1.2(1)	0.33(3)
Unassigned	0.59(5)		1.4(1)[b]	0.8(1)	0.55(6)
Grass	1.4(1)	1.06(1)	1.4(1)[b]	1.9(2)	1.5(1)
Missed/g	2.0	0.81(1)	1.40(1)	2.80(2)	1.63(2)
Isomer				17.0	5.088
QC				49.0(1.0)	29.3(7)
HK				49.5(1.0)	28.0(6)

[a]Estimate from MC calculations of the feeding of ND bands in ^{152}Dy described later in this paper.

[b]Assumed to be the same as for the identified transitions.

be of $E2$ character. If, in contrast, the A_2/A_0 value is at or below the large negative limit of -0.46, characteristic of mixed $M1/E2$ transitions [9], the corresponding A_0 channel content is considered to belong entirely to the $M1/E2$ component. For spectrum channels with A_2/A_0 values in between, the content of the QC spectrum is split proportionally, according to its position between the two limits. The $E2$ and $M1/E2$ QC spectral components determined with this approach are given in Fig. 2 along with the $E1$ statistical contribution.

The discrete peaks of Fig. 1 are from known as well as from unassigned transitions. The average multiplicities, energies, and spins removed by each component of the ^{152}Dy γ-ray ND spectrum are given in Table II. All assigned transitions
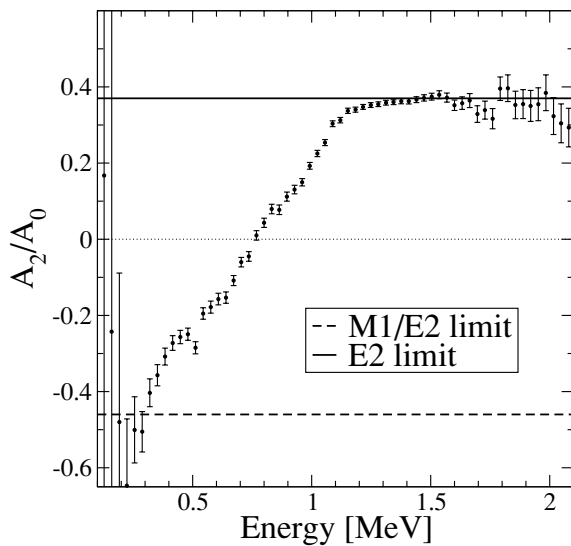

FIG. 3. Angular distribution coefficient A_2/A_0 [see Eq. (3)] for the QC spectrum of Fig. 2 *after* the fitted statistical component was subtracted.

were identified and grouped into lines above the 14-ns isomer (labeled a/14 ns in Table II) and below the isomer (b/14 ns). The remaining, very weak γ rays above the smooth QC are classified as either discrete unassigned or "grass" according to whether they could be identified as clearly separate, distinct peaks or not. The multiplicity of the grass was determined to be 1.37(8), and it was assumed that the grass, like the known discrete lines, carried 1.4(1)$\hbar$ per γ ray on average.

A small fraction of the intensity of the transitions below the 14 ns isomer will appear as a continuum because the nucleus is moving away from the target while the decay occurs, and the nominal polar angles of the GS rings are no longer correct. Such γ rays are not classified as peaks but are still collected in the QC spectra. Although they are not classified entirely properly, their intensity is, therefore, not lost.

Table II presents the spins and energies removed by all the components of Fig. 2. When the effects of isomer tagging and coincidence gating are included, Table II indicates that the mean entry point for this reaction is $I = 49.0(1.0)\hbar$ and $E = 29.3(7)$ MeV. Other measurements of the mean entry points for ^{152}Dy using different reactions have been reported [11,12] and are in good agreement with the values reported here using the ^{108}Pd(^{48}Ca,4n)^{152}Dy reaction.

IV. SUPERDEFORMED QUASICONTINUUM SPECTRUM

The 94 cleanest combinations of coincidence gates placed on the following SD band 1 transitions in ^{152}Dy [6,42] with energies 647, 693, 738, 784, 829, 876, 923, 1017, 1065, 1161, 1209, 1257, 1305, 1353, 1402, and 1449 keV, covering the spin range 28–62$\hbar$, were used to extract the total SD spectrum of γ rays presented in Fig. 4. As done for the equivalent ND spectrum in Fig. 1, the data have undergone all the same corrections and were also normalized to the number of γ cascades. The SD QC spectrum is visible under the discrete SD and ND lines. Clearly, the multiplicity of the QC
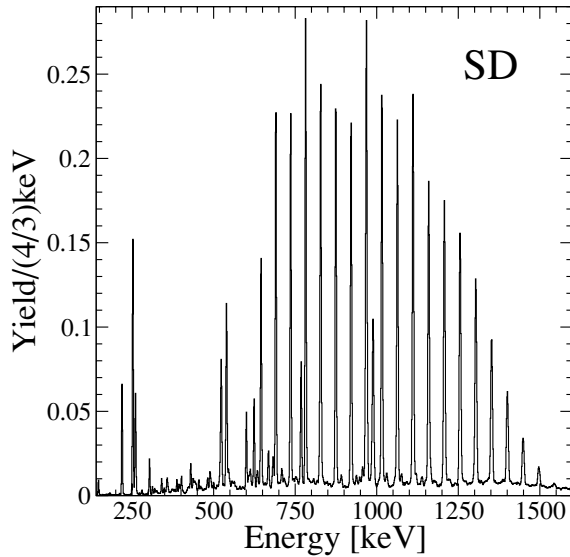
FIG. 4. Normalized γ spectrum obtained with double coincidence gates placed on clean combinations of discrete lines of SD band 1 in ^{152}Dy. The SD QC spectrum is seen under the discrete SD and ND lines. Decomposition of this spectrum is delineated in Table VI.

FIG. 5. QC spectrum of γ rays obtained when pairwise coincidence gates are set on clean combinations of lines from SD band 1 in ^{152}Dy [6]. The DO spectrum shows the MC1 calculation (see Sec. VII H) of the DO QC spectra (sum of statistical $E1$ and quadrupole $E2$ transitions), and the FEED curve is the MC1 calculation of the feeding QC spectrum. The FEED+DO curve is the sum of the two calculated QC spectra components. Also given is the subset of the FEED spectrum where the γ rays were emitted in the ND well. The dashed line provides the experimentally extracted QC spectrum after the $M1/E2$ component discussed in Sec. VIII has been subtracted.

component of the SD total spectrum is smaller than in the ND case.

For the strong discrete peaks in the SD band, the missed intensity due to gating, as well as feeding and decay, were accounted for (see details in Appendix C), and the resulting average intensity of these peaks was used to normalize the data of Fig. 4. Thus, the normalization was carried out with discrete in-band SD transitions rather than with the intensity of any discrete ND lines from the decay of the SD band.

The SD QC spectrum was extracted using the same procedure as for the ND QC component and is shown in Fig. 5. As expected, two contributions are clearly visible. MC calculations, which will be described in Sec. VII, suggest that the lower component of Fig. 5 is from the decay of the SD band, whereas the higher energy component belongs to the feeding of the SD band, with significant overlap of the two components. It should be noted that, as opposed to the $A \sim 190$ region [9], there is no sign of additional "statistical-like" QC spectrum strength at higher energies. This indicates that in the mass $A \sim 150$ region, the decay may be dominated by $E2$ transitions as opposed to $E1$ statistical transitions, partially because the decay out (DO) happens at higher spins, where $E2$ transitions are stronger. An approximate *experimental* decomposition of the QC spectra components of the SD QC spectrum in Fig. 5 will be discussed in Sec. VIII.

V. RIDGE EXTRACTIONS

Just as the QC spectra were extracted by placing double coincidence gates on ND and SD lines, 2D γ-γ matrices were accumulated using the same combinations of clean gates. In addition to double-gated matrices, single-gated and ungated matrices were generated as well so that the double-gated matrices could be background subtracted with a slightly
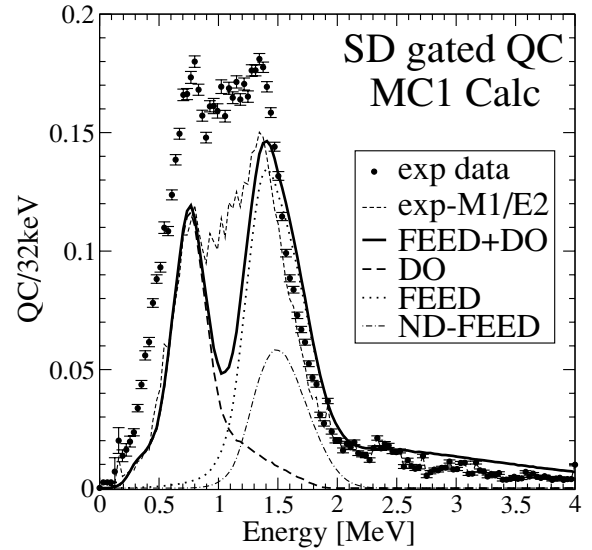
simplified version of the background subtraction method of Ref. [47], now with 2D matrices instead of 1D spectra. The 2D γ-γ matrices were updated in such a way that all increments were statistically significant; i.e., spikes from very high multiplicity events were eliminated [46] as was done for the 1D spectra. This also ensured that the statistical errors could be properly calculated and propagated.

The background-subtracted, double-gated matrices were unfolded using a 2D version (provided by D. C. Radford) of an unfolding program based on the procedure described in Ref. [48]. The matrices were then "COR subtracted" [58]; i.e., an uncorrelated matrix (but only of the relevant *local* region) was generated from a projection and subtracted so that the resulting matrix had no net counts. In the resulting matrix, positive counts represent areas where γ rays on the ordinate and abscissa axes are in strong coincidence, and negative counts are areas where these γ rays are either in weak coincidence or not in coincidence at all. Examples of the former regions are areas where discrete γ lines are in coincidence. On the other hand, as an example of the latter region, the diagonal in the matrix will in general have negative counts since γ rays tend not be in coincidence with transitions of the same energy, at least for rotors.

Before carrying out a projection of the matrix onto an axis perpendicular to the diagonal, resulting in the so-called ridge spectrum, it is important to remove any coincidence events between *discrete* lines in the region that is projected. For strong peaks, stripes along the $E_{\gamma 1}$ and $E_{\gamma 2}$ axes are quite often present

as well—even after the matrices have been unfolded. Both types of coincidences must be removed in order to improve the ridge signal with respect to the background.

In the procedure used in this work, no "repairs" are made in the 2D matrices to account for the discrete coincidence peaks and stripes that are removed. The associated areas in the matrices are simply set to zero counts. Instead, the effect of the missing matrix areas is extracted (as a "bias function" described below) and used to *correct* the cross-diagonal projections from the matrices where the stripes and peak coincidences were removed. It can be shown that the resulting ridges are very close to the true ridges (as documented in Appendix D). Nevertheless, the calculated ridges from the MC simulations, discussed below, are treated *exactly* in the same way so that any possible artifact introduced by removing peaks and stripes does not affect the comparison between the experimental data and the MC simulations. Figure 6 shows the extracted ND-gated ridges, and Fig. 7 presents the SD-gated ridges obtained in the present analysis, together with the result from MC calculations discussed in Sec. VII H. The results from the latter MC calculation for the ND gated QC is displayed in Fig. 8.

To find the "bias function," a "unity" matrix is created where all the elements have a value of unity. A cross-diagonal projection pj_1 is obtained from this matrix using the same area as was used for the diagonal projection of the ($E_{\gamma 1}$, $E_{\gamma 2}$) matrix above. Then, the same peaks and stripes are removed from the unity matrix, and a new cross-diagonal projection pj_2 is obtained. The bias spectrum is then $\mathcal{B} \equiv pj_2/pj_1$. The

FIG. 7. (Color) Ridges obtained when coincidence gates are placed on clean pairs of SD lines in ^{152}Dy. At least four narrow ridges can be seen as well as a shallow valley. The solid line is from the first MC calculation (MC1) of the ridges, discussed in Sec. VII H. The ridge represents a cut of 1450 ± 350 keV along the diagonal in the $E_{\gamma 1} \times E_{\gamma 2}$ matrix.

diagonal projection from the ($E_{\gamma 1}$, $E_{\gamma 2}$) matrix is corrected by dividing it by the $\mathcal{B}$ spectrum. It has been verified, using simulated ridges, that the corrected ridges from this procedure are very close to the true ridges, except for a scaling factor (see discussion in Appendix D).

At least four narrow ridges are clearly seen along with a shallow valley in Fig. 7. Thus, the γ cascades that feed the
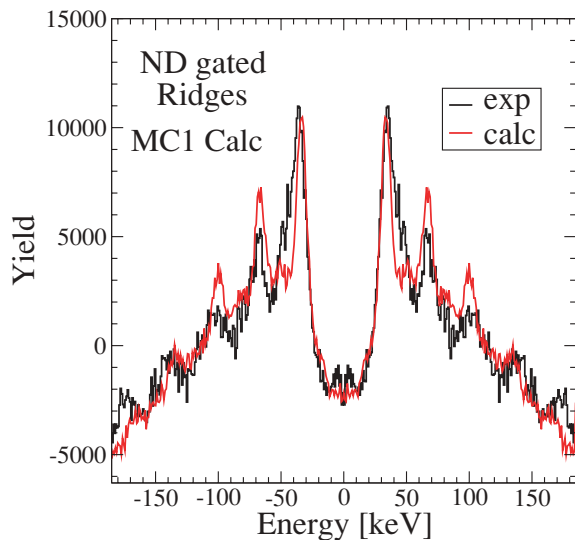

FIG. 6. (Color) Ridges obtained when coincidence gates are placed on the same ND lines in ^{152}Dy as in Fig. 1. The histogram presents experimental data. Solid red line is from the first MC calculation (MC1) of the ridges, discussed below in Sec. VII H. As discussed in the text, part of the narrow ridge structure is from γ rays emitted while the nuclear shape is prolate SD. Only the more slowly changing underlying ridge structure (particularly the valley) is from γ rays emitted when the nucleus is ND (mostly slightly oblate). The ridge represents a cut of 1450 ± 350 keV along the diagonal in the $E_{\gamma 1} \times E_{\gamma 2}$ matrix.
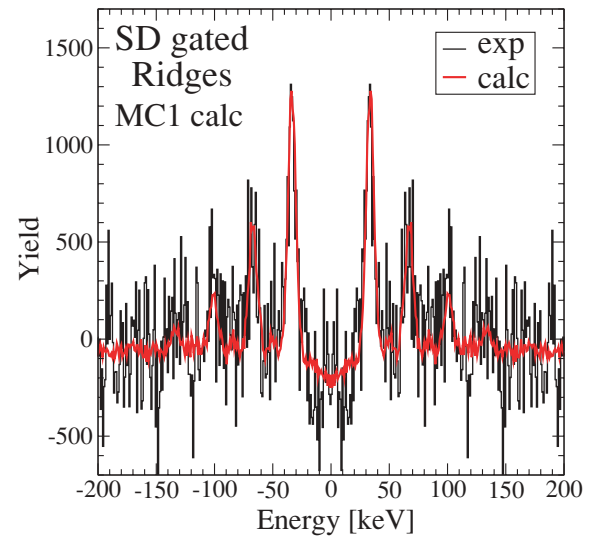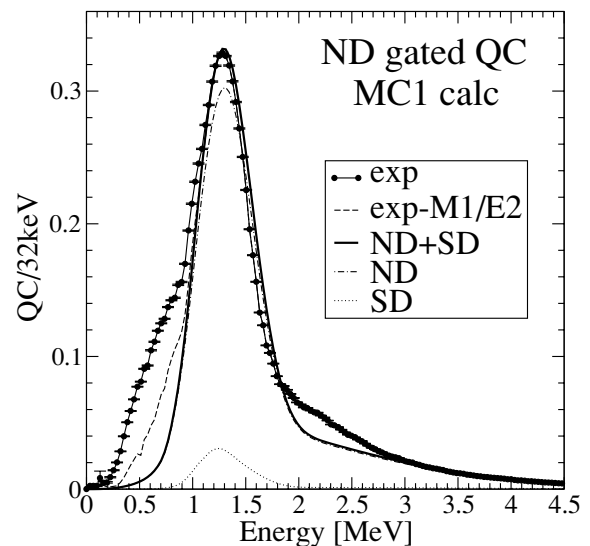

FIG. 8. QC γ rays when double coincidence gates are placed on a combination of ND transitions in the ^{152}Dy nucleus. The spectrum is similar to that reported in Refs. [11,12]. The curve marked ND (SD) indicates the γ rays emitted in the ND (SD) well, according to the MC1 calculation discussed in Sec. VII H. The dashed line provides the experimentally extracted QC spectrum after the $M1/E2$ component shown in Fig. 2 has been subtracted.

discrete SD band 1 contain a significant number of events where many γ rays are emitted in the SD well. The ND-gated ridge of Fig. 6 exhibits even more overall structure. However, the narrow width and position of the ridges as well as the ensuing MC calculations suggest that the very narrow ridge structure stems from γ rays that are emitted while the nucleus resides in the SD well.

VI. MEASURING THE TOTAL ENTRY DISTRIBUTION

A. The (H, K) extraction

In the standard GS configuration, the seven BGO detectors surrounding each Ge crystal [44] are used exclusively to suppress any γ ray scattered from the Ge crystal. The BGO detectors, therefore, are equipped with Hevimet absorbers to prevent direct hits from γ rays coming from the target, which would cause false Compton suppression. In this standard configuration, GS has a photopeak efficiency of 8.9(2)% and a total efficiency of 17.8(3)% for 100 detectors (see Appendix A).

There is another mode of operation of GS with the Hevimet absorbers removed, where the γ rays from the target (in addition to the γ rays scattered from the Ge crystals) are detected with high efficiency in the BGO counters, albeit with lower energy resolution [44]. In this mode, GS can be used as a powerful calorimeter, with a detection efficiency of 78(2)% (see Fig. 10). Furthermore, this second GS mode also provides an efficient means of measuring the γ-ray multiplicity because of the high granularity of the array. For the reaction under investigation here, there are about four times as many detector modules as the mean number of emitted γ rays (above the isomer). This makes GS suitable for the determination of the
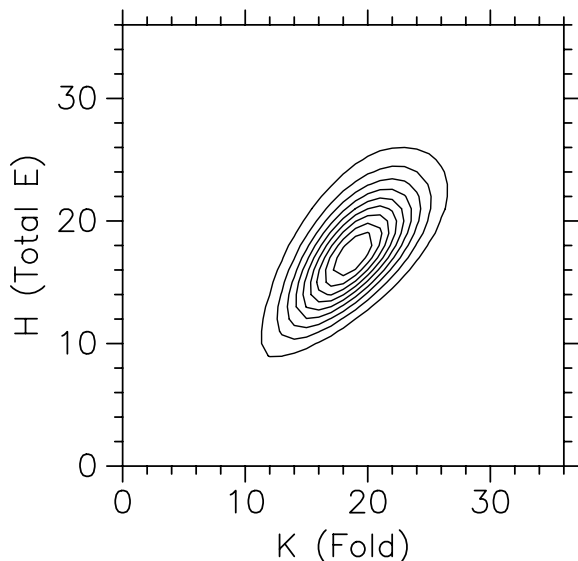

FIG. 9. Measured sum energy H vs module multiplicity K, when pairwise coincidence gates are placed on ND lines above the 17^+ isomer in ^{152}Dy. The data are background subtracted as described in the text. On the average, after isomer tagging, 19.1(4) Ge-BGO modules are hit, and a total energy of 18.1(5) MeV is detected by GS in this reaction.

entry distribution, i.e., of the location in the spin-energy plane from which γ deexcitation starts after the last particle has been evaporated. The procedure used to measure the entry distribution is described below.

Pairwise coincidence gates were placed on ND transitions in the nucleus, and the sum energy H and number K of detector modules (each comprised of a Ge crystal and seven enveloping BGO scintillator detectors) that fired were recorded. An isomer tag, as described in Ref. [9], was required as well to make the extraction of the entry distribution exclusive to the ^{152}Dy reaction channel. The 720 BGO crystals in GS were calibrated in energy so that the best possible total sum energy could be determined. Only the hit pattern and the sum energy of the seven BGO crystals in a module were available in the GS data stream. As a result, the energy calibration of the measured sum energy in a module could only be carried out exactly when single BGO crystals were hit. However, when more than one BGO crystal fired, appropriate averages of the calibration coefficients were used, based on the hit pattern.

The observed array multiplicity K and sum energy H were sorted into 2D histograms, known as (H, K) matrices. In addition to these double-gated (H, K) matrices, single-gated and ungated (H, K) matrices were collected as well, locally around each discrete double γ gate combination in the $E_{\gamma 1} \times E_{\gamma 2}$ matrix, in order to enable background subtraction using a modified version of the procedure described in Ref. [47], now with 2D (H, K) histograms instead of 1D spectra. The measured, background-subtracted, module multiplicity vs sum energy matrix is presented in Fig. 9. This distribution is, however, not the true entry distribution since corrections for the response of GS and the effect of the isomer tagging were not taken into account. The multiplicity must, moreover, be translated into the corresponding spin in order to arrive at the actual entry distribution. The procedures used to extract the entry distribution from the background-subtracted (H, K) matrix are described below.

B. The (H, K) response function

To measure the H (sum energy) and K (multiplicity) efficiency of GS, a ^{88}Y source was placed in the center of the array, and data were acquired in singles mode. This source emits two γ rays, with energies of 898 and 1836 keV, predominantly in coincidence [51]. A weak source ($\sim 2\mu$ Ci) was used in order to minimize pileup effects. Yet, this strength was sufficient to ensure that random background events were not a problem. The contribution of random events was reduced further by requiring a time coincidence. Events were subsequently selected by demanding that the photopeak of the 1836-keV ^{88}Y line was observed, hereby ensuring that the other component of such events is associated with the emission of a 898-keV γ ray in the center of GS. There is a certain probability that this 898-keV γ ray will be completely or partially absorbed in GS or will be missed altogether.

Batches of such events from 1 to 100 were added up and records kept, at each step in the batch, of the total energy observed and the number of modules hit [59]. Two-dimensional contour maps of the energy H and multiplicity K
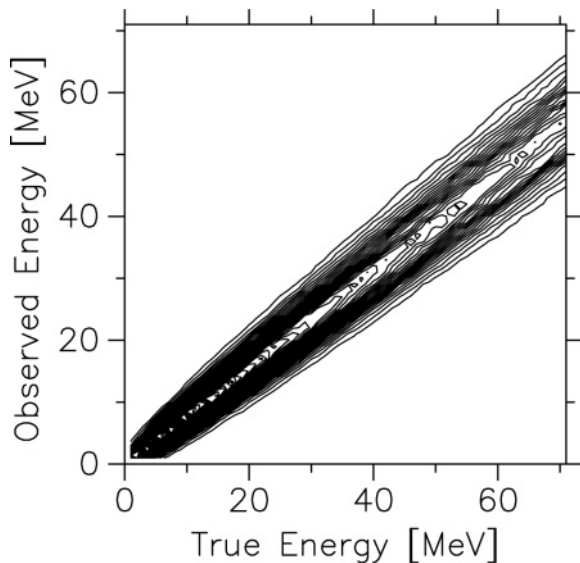
FIG. 10. Energy response H of GS, in its calorimeter mode with 100 detectors, as described in the text. The abscissa is the energy injected in GS. The ordinate gives the corresponding distribution of energy observed in GS. The contour plots indicate that the average calorimetric energy efficiency of GS is 78(2)%. The plot also presents the spread in the observed energy.

response of GS obtained in this way can be found in Figs. 10 and 11, respectively. A correction to these data was applied to take into account a small side feeding directly to the 898-keV state in ^{88}Y, i.e., bypassing the level emitting the 1836-keV line [51]. An additional small correction takes into account the fact
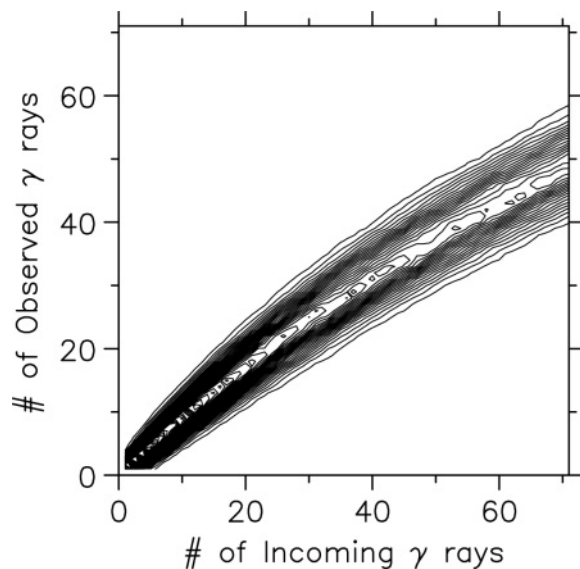

FIG. 11. Multiplicity response K of GS, in its calorimeter mode with 100 detectors, as described in the text. The abscissa is the number of γ rays emitted from the center of GS. The ordinate represents the corresponding distribution of hits in the Ge-BGO modules. As more γ rays are injected into GS, the number of multiple hits in the same modules increases. Thus, the response function curves over as the multiplicity becomes large.

that one detector in GS is used to measure the 1836-keV line. For each event generating the GS response, it is ensured that the γ rays are in coincidence with the 1836-keV transition by placing the same gates on time that were used for the observed (H, K) distribution of Fig. 9. It can be seen from Fig. 10 that GS, in its calorimeter mode, has a sum-energy efficiency of 78(2)%. In Fig. 11, the effect of multiple hits in a single module is clearly visible as a deviation of the response function from a straight line at higher multiplicities. A competing effect originates from events where one γ ray scatters from a Ge-BGO module into a neighbor, thus producing two hits. Such effects and any others are taken into account through the measured response functions.

The mean energy of all ^{152}Dy γ rays of Fig. 1 is $\sim$1130 keV after the data have been corrected for γ rays missing due to the effect of gating, but not for internal conversion. The latter correction would add to the multiplicity but lower the mean energy slightly. This justifies the use of the ^{88}Y 898-keV γ ray to measure the response function. In addition, a Monte Carlo N-particle transport code (MCNP) simulation [60] of the Ge-BGO modules indicates that the total efficiency is nearly constant over the range $\sim$0.6–1.8 MeV. Thus, the simulated GS calorimetric efficiency changes by at most a few percent over this range.

C. The (H, K) unfolding

The unfolding of the measured (H, K) distribution, shown in Fig. 9, is carried out following an MC-based procedure described in Ref. [59]. From an initial guess of an entry distribution, random E (sum energy) and M (multiplicity) points are selected in 2D, and the response functions provided in Figs. 10 and 11 are used to fold these (E, M) entries into what would be observed in GS in terms of the number of modules (also referred to as fold) K and the observed sum energy H. Thus, for each value of M and E, the observed K and H are selected (randomly) from the 1D ordinate projections in Figs. 10 and 11 corresponding to the appropriate abscissa for E and M. It follows that in addition to accounting for the finite efficiency for observing the multiplicity and total energy of a γ-ray cascade in GS, this folding adds the spread in K and H reflected in the response functions. If the point folded in this way falls inside the observed (H, K) distribution, (i) the selected (M, E) point is stored in the next generation, improved (M, E) entry distribution and (ii) one is subtracted from the observed (H, K) distribution in the particular (H, K) location that was selected. On the other hand, if the observed entry distribution does not contain any counts (or does not have any counts left at this point in the folding/unfolding procedure) in the selected (H, K) channel, then nothing is done, and a new random M and E point is selected and the same procedure is repeated.

When all (or nearly all) of the counts in the observed (H, K) distribution have been selected (eliminated) in this MC procedure, the next generation (M, E) distribution that was accumulated in the process represents a better approximation to the true (M, E) entry distribution. The process is then repeated with the same MC procedure described

above, and an even better, true (M, E) entry distribution is generated. This iterative procedure quickly converges toward a final, best approximation to the (M, E) entry distribution that folds into the measured (H, K) entry distribution of Fig. 9.

The initial guess of an entry distribution is usually taken to be a simple, flat, unbiased distribution in M and E, and from five to ten iterations of the MC unfolding procedure are performed. One should be aware that it is not possible to find a unique distribution that is the true (M, E) entry distribution from the measured (H, K) distribution in GS. However, it is expected that the (M, E) distribution found in the MC unfolding procedure described above (Fig. 12) is a fair representation of the (M, E) distribution that would be observed in an ideal calorimeter with 100% efficiency and infinite granularity of γ-ray detectors.

D. Normal deformed (I, E) entry distribution

To arrive at the final (I, E) entry distribution for the ^{48}Ca$+^{108}$Pd reaction, the effect of the isomer tagging has to be taken into account, and the multiplicity dimension of the measured multiplicity–sum-energy (M, E) distribution of Fig. 12 must be translated into the associated spin–total-energy distribution. This can be done by inspecting Table II. The mean spin removed by observed γ rays (above the isomer) is 32.0(4), and their multiplicity is 22.0(1). Thus, the mean spin removed per *observed* γ ray in GS is 1.45(3)$\hbar$, and the conversion of M to I is $I = 1.45(3) \times M$, in good agreement with Refs. [11,12]. To arrive at the complete (I, E) entry distribution, one must also add the effect of tagging on the isomer. It follows that the complete (I, E) entry distribution is derived from the unfolded
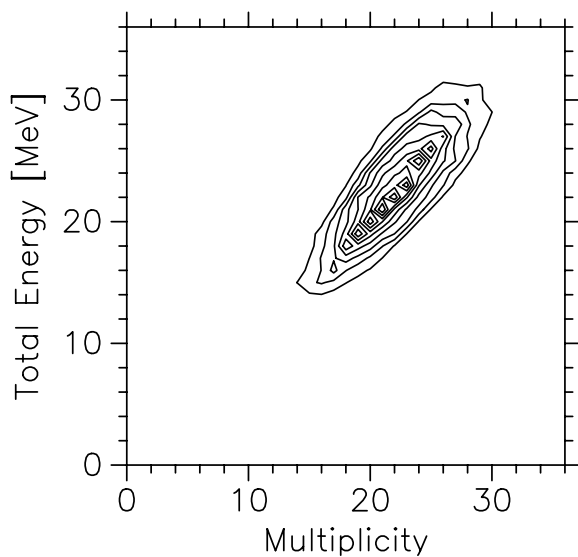

FIG. 12. (M, E) distribution from the unfolded (H, K) distribution of Fig. 9. The mean multiplicity is 22.3(5) and the mean energy is 23.2(6) MeV.
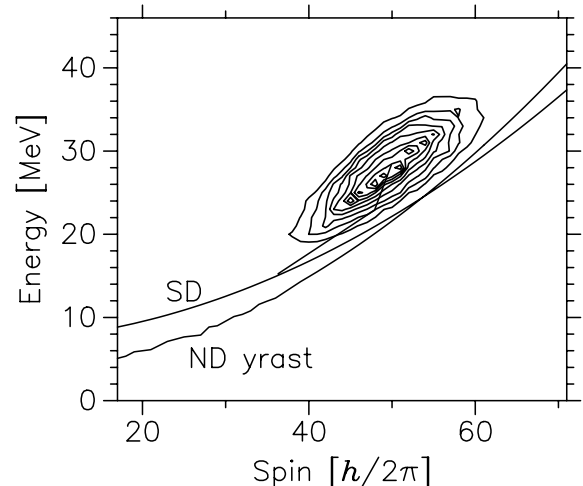

FIG. 13. Measured (I, E) entry distribution for the γ cascades feeding ND states above the 17^+ isomer in ^{152}Dy. The two lines are the ND and SD yrast lines used in the MC calculations described below. The line starting at the center of the entry distribution indicates the calculated mean decay vectors for the statistical and quadrupole transition components of the QC of γ rays (from the MC2 calculation discussed in Sec. VII I). The mean entry spin and energy are 49.5(1.0)$\hbar$ and 28.0(6) MeV, respectively.

(M, E) distribution as

$$I = 1.45(3) \times M + 17.0, \tag{5}$$

$$E = E + 5.088, \tag{6}$$

where the units are $\hbar$ and MeV, respectively, since the isomeric state has a spin of 17$\hbar$ and an energy of 5.088 MeV. The final (I, E) entry distribution for the ^{152}Dy channel in this reaction, under the gating conditions used, is presented in Fig. 13 along with the ND and SD yrast lines that were used in the MC calculations described below. The mean entry spin and energy are measured to be 49.5(1.0)$\hbar$ and 28.0(6) MeV, in excellent agreement with the mean values obtained from the QC spectrum analysis presented in Table II. With respect to the ND yrast line, the mean feeding excitation energy over the ND yrast line, U, is 7.0(6) MeV, which is quite consistent with the neutron binding energy of 9.4 MeV [61].

VII. MONTE CARLO CALCULATIONS

A. Introduction

A Monte Carlo (MC) calculation is used to *simultaneously* reproduce both the QC spectra of Figs. 2 and 5 and the correlation ridges of Figs. 6 and 7. As was mentioned in the Introduction, the MC calculation contains the rotational damping parameters Γ_μ, $\Gamma_{rot}^{(2)}$, and I_{nar} for the SD and ND wells. Thus, reproducing the experimentally measured QC spectra and ridges constitutes a determination of the rotational damping in the two wells—within the validity of the model.

MC simulations based on the model outlined below were previously used successfully to describe data on (SD) nuclei in the mass $A \sim 190$ region [9]. As a matter of fact, simulations

with this model placed constraints on the excitation energy and spin of SD bands at a time when discrete transitions linking the SD bands to the ND states they decay into had not yet been observed [62]. The present code is based on an earlier, much simpler version which only handled deexcitations in the ND well [11,12]. It is worth noting that an independent MC calculation of the QC in ^{152}Dy has been presented by Schiffer *et al.* [13].

For the present work, the MC code was improved to handle the two components of the damping, Γ_μ and $\Gamma_{\rm rot}^{(2)}$, which theory [24] now suggests are necessary to reproduce the observed ridges of Figs. 6 and 7. The calculation follows the γ cascades from the measured entry distribution until they come close ($\sim$1 MeV) to either the ND or SD yrast line. At this particular point of the decay, $M1/E2$ γ rays are predominantly emitted in the last few steps linking the QC to the discrete states [9]. These last-step γ transitions are not included in the MC simulations. A brief outline of the model calculations is given below; additional details are presented in the following subsections.

For each step in the γ decay, a total of eight decay widths are calculated, namely, those associated with quadrupole $E2$ transitions ($\Delta I = 2$) and statistical $E1$ transitions ($\Delta I = -1, 0, 1$) in both the ND and SD wells. If the nucleus is SD at the time of decay, the four decay widths in the ND well are attenuated by the penetration probability through the barrier that separates the levels in the two wells. The attenuation is large if the SD state resides deep in the SD well, and near unity at the top of the barrier. Conversely, if the nucleus occupies a state in the ND well, the four calculated decay widths in the SD well are attenuated. The subsequent decay path is selected in a MC fashion from values of the eight decay widths. If a ND(SD) decay width is selected, the decay occurs in the ND(SD) well.

For $E2$ transitions, the wide or narrow damping component is first selected based on the value of the $I_{\rm nar}$ parameter. An additional deviation with a Gaussian shape around the mean γ transition energy [Eq. (20) below] is then added, with a width based on the input value of the rotational damping widths, Γ_μ or $\Gamma_{\rm rot}^{(2)}$. This step is actually done before the final $E2$ decay widths are calculated, since the E^5 term in the decay width formula [see Eq. (19) below] strongly favors the $E2$ deexcitations where the (mostly) wide component adds to the decay γ-ray energy, giving rise to a very important *additional cooling* of the γ cascades.

In this work, Γ_μ, $\Gamma_{\rm rot}^{(2)}$, and $I_{\rm nar}$ are considered to be independent parameters. Thus, the correlation between Γ_μ and $\Gamma_{\rm rot}^{(2)}$ that is often implicit in theory, see, e.g., Ref. [15], is ignored. This is justified since rotational damping is, in principle, independent of compound damping [24]. As was discussed in the Introduction, the origins of Γ_μ and $\Gamma_{\rm rot}^{(2)}$ are different, with $\hbar/\Gamma_\mu$ representing the mean time that the nucleus spends in an intrinsic configuration and $\hbar/\Gamma_{\rm rot}^{(2)}$ the mean time that it takes a state to get distributed over the compound eigenstates [20]. The approach in this work is to independently vary Γ_μ, $\Gamma_{\rm rot}^{(2)}$, and $I_{\rm nar}$, either as values independent of I and U (in the MC1 calculation in Sec. VII H) or as renormalized functions (MC2 in Sec. VII I), until the best

simultaneous fit to the measured ND and SD ridges and QC spectra (four spectra in total) is found.

In the simulations, the γ rays in the cascades are binned, forming the calculated QC spectra displayed in Figs. 2 and 5. For the ND spectrum of Fig. 2, all calculated γ cascades are used independent of the well they were trapped in. For the SD QC spectrum (Fig. 5), only cascades trapped in the SD well are considered. The latter happens about 1–2% of the time [5]. The MC calculations also reproduce this feeding intensity of the discrete SD bands. As a matter of fact, $E_{\rm bs}$, the height of the barrier separating the SD from the ND well [see Eq. (39) below] is adjusted to get the proper feeding of the SD band in the simulations.

The calculated γ-γ coincidences in the cascades are binned in 2D γ-γ matrices after correcting for the experimental detector efficiency. These simulated matrices are processed in *exactly* the same way as the measured data; i.e., peaks and stripes are removed (even though discrete peaks are not included in the model), and a COR subtraction is performed [58]. Subsequently, the calculated ridge spectra are extracted by projecting the simulations on an axis perpendicular to the diagonal for the *same* γ energy region as the experimental matrices. Figures. 6 and 7 present the simulated ridges obtained in this way.

The following subsections give more details about how the cooling of the nucleus toward the ND and SD lines, by emission of QC γ rays, is treated in the model. In this work, the mixing theory of Vigezzi *et al.* [63,64] is used. Another approach has been proposed by Weidenmuller *et al.* [65–67], and the two methods have been discussed in detail by Stafford and Barrett [68]. The Vigezzi model is expected to be more appropriate in the regime of finite temperatures ($U > 1$ MeV), e.g., in the regime for which the QC γ rays are calculated in the MC simulations, because Fermi's golden rule applies here.

B. Yrast lines

To perform the MC calculations, both the ND and SD yrast lines must be extrapolated beyond the known states toward higher spin. For the SD band, this is done by fitting the known yrast levels to the functional form

$$E(I) = E(0^+) + a[I(I+1)] + b[I(I+1)]^2, \qquad (7)$$

and using the fitted values beyond a spin of $66\hbar$. The yrast energies corresponding to the odd spins are determined from this fit as well. This procedure is straightforward, and barring any irregularities in the feeding region due to alignments (for example), the extrapolated SD yrast line is quite reliable in the spin range covered by the entry distribution. On the other hand, the ND yrast line is less well known. Indeed, above a spin value of $\sim$38$\hbar$, information on the ^{152}Dy ND level scheme is more fragmentary. Work is currently in progress to extend the level scheme beyond spin 38$\hbar$ using the present data set [69], with the potential of reducing the uncertainties inherent in the determination of the ND yrast line used here. Preliminary results identify part of the yrast line at high spins. All in all, to extend the ND yrast line beyond spin 38$\hbar$, a fit was carried out with the functional form of Eq. (7) to the

lowest known energy levels with the spins 14–38$\hbar$. Three states near spin 50$\hbar$, from the preliminary level scheme mentioned above, were included as well to improve the reliability of the fitted yrast line at higher spins. The levels below spin 14$\hbar$ are excluded from the fit, since they are clearly lowered in energy by pairing effects. The resulting ND yrast line, presented in Fig. 13 (along with the SD yrast line) for spin $\geqslant 38\hbar$, is from this fit. This approach suggests that the ND yrast line crosses the SD yrast line around spin $\sim 54\hbar$, in excellent agreement with the theoretical predictions of Refs. [70,71].

C. Entry point and initial shape selection

Each γ cascade in the MC simulation is started by randomly selecting a spin and excitation energy according to the *measured* entry distribution of Fig. 13. Because a measured entry distribution is used, the competition with fission at large angular momenta is automatically accounted for.

The initial shape of the nucleus is selected according to the ratio of level densities in the ND and SD wells at the selected entry point. Thus, if ρ_{SD} and ρ_{ND} are the level densities in the two wells, for the selected (I, E) point, the probability for occupation of the SD well is taken to be

$$P_{SD}(\text{initial}) = \frac{\rho_s(U_{SD})}{\rho_s(U_{SD}) + \rho_{ND}(U_{ND})}, \qquad (8)$$

where U_{ND} and U_{SD} are the excitation energies above the ND and SD yrast lines, respectively. The level densities are calculated using Eq. (9) below, with parameters explicitly specified for the two wells.

The level density for definite values of the spin and parity can be evaluated as [13,72,73]

$$\rho_I(U) = \frac{(2I+1)\sqrt{a}}{24}\left(\frac{\hbar^2}{2\Im_r}\right)^{3/2}\frac{e^{2\sqrt{a(U-\Delta)}}}{(U - \Delta + U')^2}, \qquad (9)$$

where I is the spin of the level and U the excitation energy above the yrast line. In this so-called back-shifted Fermi gas model (BFSG) expression, the back-shift parameter, which stems from pairing [74], is denoted by Δ and causes the level density to approach zero for $U \to \Delta$. Other possible choices of level density formulas are discussed in Appendix F. The $(2I + 1)$ scaling with spin breaks down at high spins [75]. However, the particular choice of level density formula in the MC calculations is not expected to be critical for the extraction of the rotational damping values. No energy dependence of Δ was considered in the calculations described here.

Systematics of the value of Δ at zero spin can be found on p. 170 in Ref. [74] ($\Delta \sim 24/\sqrt{A}$ MeV for even-even nuclei). At higher spins, the pairing is quenched [76]. The level density parameter is denoted by a, and systematics of the value of this parameter is given on p. 187 in Ref. [74]. For the Dy region, $a \sim A/7$ MeV^{-1} [11,12] is used; the general trend for a wider mass region is $a \sim A/8$ MeV^{-1} (see also Ref. [77]). Thus, in this work, a was set to 21.7 MeV^{-1} in the ND well. There are several indications that the level density in the SD well is smaller than in the ND well (see, e.g., [70]). Based on

fits to experimental data, Schiffer *et al.* [13] suggest that $a \sim A/10$ MeV^{-1} is more appropriate in the SD well. Thus, a value of 15.2 MeV^{-1} for the level density parameter in the SD well is adopted in this work. The U' parameter used in Eq. (9),

$$U' = \frac{3}{2}\left(\sqrt{\frac{U}{a} + \frac{9}{16a^2}} + \frac{3}{4a}\right), \qquad (10)$$

is related to the thermodynamical temperature of the Fermi gas [73,77] and is included to improve the behavior of the level density formula at low excitation energies. The *rigid* moment of inertia is denoted $\Im_r$, and for low deformation, it is evaluated as (Ref. [74], p. 75)

$$\Im_r = 0.0276\, A^{5/3}\left(1 + \tfrac{1}{3}\delta\right)[\hbar^2/\text{MeV}]; \quad \delta \equiv 0.946\,\beta_2, \qquad (11)$$

where β_2 is the nuclear quadrupole deformation parameter. For larger deformation, the expression from Ref. [78] is used, that is,

$$\Im_\kappa = 1.37610^{-2}A^{5/3}\left[1 - \sqrt{\frac{5}{4\pi}}\beta\cos\left(\gamma - \frac{2\pi}{3}\kappa\right)\right], \qquad (12)$$

where $\Im_\kappa$ is in units of $\hbar^2/\text{MeV}$, and κ takes the values 1, 2, and 3 according to the axis around which the rotation takes place. For prolate nuclei, with no triaxiality (i.e., $\gamma = 0$), $\kappa = 3$ corresponds to the quantum-mechanically forbidden rotation about the symmetry axis ($\Im_z$). With $\kappa = 1, 2$ the rotation takes place around the short axis of the nucleus. The latter rotation is associated with $\Im_r$ in Eq. (11).

The MC code is also used to calculate the DO QC spectrum which takes place from the bottom of the SD band toward the states near the ND yrast line. This is accomplished by simply replacing the (I, E) entry distribution described above with the discrete points in the (I, E) plane from which the decay of SD band 1 occurs. In the MC process, the initial entry point is selected randomly according to the experimentally observed decay branch. Except for this special discrete entry distribution, the MC calculations are carried out in exactly the same way. Thus, the *same* MC simulation consistently handles both the feeding *and* decay of SD bands.

D. Statistical decay

The total radiative decay width for a statistical $E1$ transition can be written as the sum of the $\Delta J = \pm 1, 0$ decay widths, that is,

$$\overline{\Gamma}_{E1} = \sum_{I=J-1}^{J+1} \overline{\Gamma}_{E1}^I,$$

$$\overline{\Gamma}_{E1}^I = \int_0^{E_\lambda^I} E_\gamma^3 f_{E1}(E_\gamma)\frac{\rho_I(E_\lambda - E_\gamma)}{\rho_J(E_\lambda)}\, dE_\gamma, \qquad (13)$$

where E_λ^I is the maximum transition energy, E_γ the energy of the γ ray, and J and I the spins of the initial and final states,

respectively. The level density is denoted by ρ [Eq. (9)], and the γ strength function $f_{E1}(E_\gamma)$ is taken to be of the Lorentzian form [79–83]

$$
\begin{aligned}
f_{E1}(E_\gamma) = {}& 3.29 \times 10^{-6} \times \frac{NZ}{A}(1 + 0.8x) \\
& \times \frac{E_\gamma \Gamma_{\text{GDR}}}{\left(E_\gamma^2 - E_{\text{GDR}}^2\right)^2 + \Gamma_{\text{GDR}}^2 E_\gamma^2}
\end{aligned}
\tag{14}
$$

for spherical nuclei. A more realistic decay strength function (described below) is used for deformed nuclei in the MC code. N and Z are the number of neutrons and protons in the fusion evaporation residue, and E_{GDR} and Γ_{GDR} represent the mean energy and width of the giant dipole resonance (GDR). The factor x is the fraction of exchange forces present in the nuclear force, assumed to be 1/2 in this treatment [84]. A number of temperature-dependent $E1$ strength functions have been proposed, see Refs. [82,83,85,86]. However, only the standard $E1$ strength function, first proposed by Axel [79], has been used in this work.

If a partial decay width $\Gamma_{E1}^p(E_\gamma)$ is defined as

$$
\Gamma_{E1}^p(E_\gamma) = E_\gamma^3 f_{E1}(E_\gamma)\frac{\rho_I(E_\lambda - E_\gamma)}{\rho_J(E_\lambda)},
\tag{15}
$$

it is seen that the total decay width in Eq. (13) can be written as

$$
\overline{\Gamma}_{E1} = \sum_{I=J-1}^{J+1} \int_0^{E\lambda} \Gamma_{E1}^p(E_\gamma)dE_\gamma.
\tag{16}
$$

Moreover, the spectral distribution of the statistical γ rays can be written as

$$
\nu_{E1}^J(E_\gamma)dE_\gamma = \frac{\Gamma_{E1}^p(E_\gamma)}{\overline{\Gamma}_{E1}}dE_\gamma.
\tag{17}
$$

The upper integration limit E_λ in Eq (16) is determined as

$$
E_\lambda = U \pm \frac{\hbar^2}{\mathfrak{I}^{(1)}}I, \quad I = J \mp 1, \quad E_\lambda = U, \quad I = J,
\tag{18}
$$

where U is the excitation energy above the yrast line for the excited state with spin J. The symbol $\mathfrak{I}^{(1)}$ represents the static (not rigid) moment of inertia, which is different for the two possible shapes (ND and SD).

E. Collective decay

Rotational damping ([14,15]) can be incorporated into the collective (stretched) $E2$ decay by the addition of a Gaussian spread in the γ-ray energy. This yields a partial decay width in analogy to Eq. (15) of

$$
\begin{aligned}
\Gamma_{E2}^p(E_\gamma) \, [\text{MeV}] = {}& E_\gamma^5 \frac{Q^2[e\,\text{fm}^2]\langle J020|(J-2)0\rangle^2}{1.25 \times 10^{13}} \\
& \times \frac{1}{\sqrt{2\pi}\,\sigma_{\text{rot}}} e^{\frac{(E_\gamma - \overline{E_\gamma})^2}{2\sigma_{\text{rot}}^2}},
\end{aligned}
\tag{19}
$$

where $\overline{E_\gamma}$ is the collective $E2$ mean γ energy

$$
\overline{E_\gamma} = \frac{\hbar^2(2J-1)}{\mathfrak{I}^{(1)}},
\tag{20}
$$

and the rotational damping width is either $\sigma_{\text{rot}} = 0.8493 \times \Gamma_\mu$ or $0.8493 \times \Gamma_{\text{rot}}^{(2)}$, depending on whether the narrow or wide rotational damping width is selected. The nuclear quadrupole moment is denoted by Q (see also Ref. [87]). The $\mathfrak{I}^{(1)}$ moment in Eqs. (18) and (20) is not necessarily the rigid moment of Eq. (11). The static moment of inertia $\mathfrak{I}^{(1)}$ is adjusted to reproduce the energy spacing between the center of the valley and the first ridge in the ridge spectra and the mean energy of the $E2$ component of the QC spectrum.

The total decay width for the collective $E2$ transition is thus

$$
\overline{\Gamma}_{E2} = \int_0^{E_{\max}} \Gamma_{E2}^p(E_\gamma)dE_\gamma, \quad E_{\max} = U + \frac{\hbar^2(2J-1)}{\mathfrak{I}^{(1)}};
\tag{21}
$$

and the spectral distribution is

$$
\nu_{E2}^J(E_\gamma)\,dE_\gamma = \frac{\Gamma_{E2}^p(E_\gamma)}{\overline{\Gamma}_{E2}}\,dE_\gamma.
\tag{22}
$$

It should be noted that if the moments of inertia $\mathfrak{I}^{(1)}$ describing the states on the yrast line and in the QC are equal, then in the absence of rotational damping, an $E2$ γ decay will *not* cool the nucleus. In contrast, if rotational damping is included, then the $E2$ transitions will on average cool the cascade with respect to the yrast line because of the E_γ^5 term in Eq. (19). This cooling is, however, less than that accomplished by $E1$ transitions. The MC calculations clearly indicate that the γ cascades must pass through a region where $\Gamma_{\text{rot}}^{(2)}$ is substantial compared to the mean γ-ray energy [see Eq. (20)]. Otherwise, the reproduction of the QC spectra would require that the γ deexcitation be terminated at unrealistically high excitation energies above the yrast line.

F. Giant dipole resonance strength function for deformed nuclei

In this work, the GDR strength function in Eq. (14) is evaluated with the following adopted GDR parameters [88,89]:

$$
E_{\text{GDR}} \, [\text{MeV}] = \frac{40}{A^{1/3}} + 7.5,
\tag{23}
$$

$$
\Gamma_{\text{GDR}} \, [\text{MeV}] = 0.029 * E_{\text{GDR}}^{1.6}.
\tag{24}
$$

These values are appropriate for spherical nuclei. For deformed nuclei, the symmetry is broken, and the GDR strength function parameters depend on the quadrupole deformation parameter,

β_2, and asymmetry parameter, γ, as [88]

$$\delta^i = \sqrt{\frac{5}{4\pi}} \beta_2 * \cos\left(\gamma + 2\frac{\pi}{3}i\right), \qquad (25)$$

$$E_{\text{GDR}}^i = E_{\text{GDR}} * e^{-\delta^i}, \qquad (26)$$

$$\Gamma_{\text{GDR}}^i = \Gamma_{\text{GDR}} \left(\frac{E_{\text{GDR}}^i}{E_{\text{GDR}}}\right)^{\delta^i}, \qquad (27)$$

$$f_{E1}^i(E_\gamma) = 3.29 10^{-6} \times \frac{NZ}{A}(1 + 0.8x) \qquad (28)$$

$$\times \frac{E_\gamma \Gamma_{\text{GDR}}^i}{\left(E_\gamma^2 - \left(E_{\text{GDR}}^i\right)^2\right)^2 + \left(\Gamma_{\text{GDR}}^i\right)^2 \left(E_\gamma^i\right)^2}, \qquad (29)$$

where $i \in \{1, 2, 3\}$ and refers to the three principal axes of the nucleus. The total strength function is then the sum

$$f_{E1}(E_\gamma) = \sum_{i=1,2,3} w(i) f_{E1}^i(E_\gamma), \qquad (30)$$

where the weights, $w(i)$, are determined as

$$w(i) = \frac{w^o}{3 * A_r(i)}, \qquad (31)$$

$$A_r(i) = \int f_{E1}^i(E_\gamma) dE_\gamma, \qquad (32)$$

with w^o being the integral of the spherical strength function in Eq. (14). To render the ND and SD strength functions even more realistic, they are generated as energy weighted sums over appropriate areas of the (β_2, γ) potential energy planes for the ^{152}Dy nucleus in either its ND or SD shape. Figure 14 provides the final strength functions used in the MC calculations. Note how the long axis of ^{152}Dy in its SD shape brings down the lowest component in the SD GDR strength function and, correspondingly, the two shorter axes give rise to the strength at higher energy.
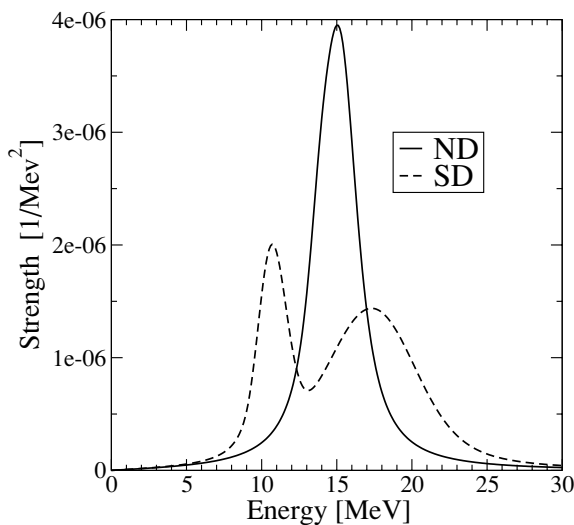

FIG. 14. ND and SD GDR strength functions used in MC calculations [see Eq. (30)].

G. γ-decay selection

For simplicity, let the decay widths associated with the eight possible γ deexcitation decays be denoted as: $\Gamma(1), \Gamma(2), \ldots, \Gamma(8)$, where 1, 2, 3 relate to the $E1$ decay widths in the ND well, 4 is the $E2$ decay width in the ND well, and indexes 5 to 8 likewise characterize the $E1$ and $E2$ decay widths in the SD well. A total decay width can then be calculated as

$$\Gamma(\text{total}) = p_1 \sum_{i=1}^{4} \Gamma(i) + p_2 \sum_{i=5}^{8} \Gamma(i), \qquad (33)$$

$$p_1 + p_2 = 1, \qquad (34)$$

where the weight factors p_1 and p_2 are determined by the mixing between the states in the SD and ND wells. The weight factors explicitly depend on the well from which the γ decay takes place, i.e., whether the deexciting level is in the SD or in the ND well.

To calculate the p_1 and p_2 parameters, the mixing theory developed by Vigezzi *et al.* [63,64] is used in this work. In this approach, the probability for decay out of the SD well, N_{out}, is calculated assuming that the nucleus starts from the ground state in the SD well. In this theory, the decay out probability N_{out} depends only on two quantities: (i) the ratio

$$\frac{\Gamma}{D} = \frac{\Gamma}{D_{\text{ND}}}, \quad D_{\text{ND}} = \frac{1}{\rho_{\text{ND}}(U_{\text{ND}})}, \qquad (35)$$

where D_{ND} is the mean distance between levels in the normal well, while Γ is a (tunneling) spreading width; and (ii) the ratio of the decay widths in the two wells:

$$\frac{\Gamma_{\text{ND}}}{\Gamma_{\text{SD}}} = \sum_{i=1}^{4} \Gamma(i) \left/ \sum_{i=5}^{8} \Gamma(i). \right. \qquad (36)$$

The coupling between the SD level and the ND states, v, is found by equating the spreading width from Fermi's golden rule Γ and the tunneling width Γ_{tunn} [63]:

$$\Gamma = \frac{2\pi v^2}{D_{\text{ND}}}, \quad \Gamma_{\text{tunn}} = \frac{\hbar \omega_s T}{2\pi} \qquad (37)$$

$$\Rightarrow v \approx \sqrt{\frac{\hbar \omega_s D_{\text{ND}} T}{4\pi^2}}, \qquad (38)$$

where ω_s is the tunneling frequency and T is the transmission coefficient through the barrier separating the two wells. The transmission coefficient is taken to be (see Refs. [90] and [91], p. 746)

$$T = \frac{1}{1 + e^\gamma}, \quad \gamma = \frac{2\pi(E_{\text{bs}} - E)}{\hbar \omega_b}. \qquad (39)$$

This is the so-called inverted parabolic barrier approximation. The parameter $\hbar \omega_b$ is always assumed to be 0.6 MeV in this work, typical of what is used in Ref. [91] (see also Ref. [71]; changing $\hbar \omega_b$ effectively translates into a renormalization of E_{bs}). The barrier height, which is measured from the bottom of the SD well, is considered to be a function of spin, that is,

$$E_{\text{bs}}(I) [\text{MeV}] = (I[\hbar] - 15) \times 0.061 + 0.12 [\text{MeV}], \qquad (40)$$

within the feeding and DO regions covered by the MC calculations. The parameters in Eq. (40) were chosen so that E_{bs} is ∼0.7 MeV in the spin region ∼20–29ℏ, where SD band 1 decays out of the SD well [6,92]. On the other hand, the slope used in Eq. (40) was adjusted so that in the ∼42–66ℏ spin region, where SD band 1 is fed, the MC simulations reproduce the experimentally observed SD population probability of ∼2% [93]. The MC calculation suggests that, in the latter region, the barrier height E_{bs} is of the order of ∼2.5 MeV.

In this work, E_{bs} is considered to be independent of the excitation energy. In reality, however, the shell effects responsible for the barrier are expected to vanish at higher excitation energies; e.g., Ref. [76] suggests that the barrier is about 2.5 MeV at zero excitation energy and vanishes at a temperature $T = 0.7$ MeV in the feeding region. The temperature is related to the excitation energy U as $T = \sqrt{U/a}$ [15,94]. Thus, for the present case, E_{bs} is evaluated to be ∼0 at $U = 7.5$ MeV, which is just above the value associated with the entry distribution, 7.0(6) MeV (see Sec. VI D). The effective E_{bs} value for the γ cascades might then be expected to be of the order of 1–2 MeV in the feeding region, in reasonable agreement with the ∼2.5 MeV used in these MC calculations. In Ref. [71], the barrier is calculated to be ∼2.9 MeV at spin ∼56ℏ, in good agreement with 2.6 MeV from Eq. (40).

In this MC model, N_{out}, the probability for decay out of the SD well, is calculated by placing the initial SD (ND) level in the middle of a distribution of 99 ND (SD) levels with a GOE having a mean level spacing of D_{ND} (D_{SD}) [14,39]. This is done by first finding the eigenvalues of a matrix with on-diagonal elements having a variance of $2\sigma^2$ and off-diagonal elements having a variance of σ^2, where σ is randomly selected from Gaussian distributions with a spread of $D_{ND,SD}\sqrt{99}/\pi$ (i.e., the final states are assumed to be fully chaotic in nature). The SD (ND) state, $|1\rangle$, is then placed in the middle of the GOE distribution, and the coupling between the SD (ND) and ND (SD) states is turned on: $|\langle n|1\rangle|^2 = v^2$ for $n \neq 1$, and $|\langle n|j\rangle| = 0$ for $j \neq i \neq 1$. The system is diagonalized and the component of the SD (ND) state, $|1\rangle$, in the resulting eigenvectors, $c(i)$, determines N_{out} as [63,64]

$$N_{out} = \sum_i |c(i)|^2 \frac{(1 - |c(i)|^2)}{(1 - |c(i)|^2) + |c(i)|^2 \Gamma_{SD}/\Gamma_{ND}} \quad (41)$$

for a decay from the SD well to the ND well. For a decay from the ND well to the SD well, the same expression applies, but Γ_{ND}/Γ_{SD} is used instead of Γ_{SD}/Γ_{ND}.

It follows that p_1 and p_2, in addition to Γ/D_{ND} (Γ/D_{SD}) and Γ_{ND}/Γ_{SD}, also depend on the particular GOE ensemble that was selected. A large number of random GOE ensembles are used in the MC calculations to effectively average over this dependence. For $\Gamma/D < 0.001$, the spreading width is so low that a simple two-level model is used; for $\Gamma/D > 20$, the 100 levels used in the diagonalization are no longer sufficient, and a Breit-Wigner approximation is used instead [63,64].

The symbol v in Eq. (38) represents the coupling strength between the SD state located at the *bottom* of the SD well and the levels in the ND well. A more general expression for v,

applicable to all states in the SD well, is ([91], p. 768)

$$v \approx \sqrt{\frac{D_{SD}D_{ND}T}{4\pi^2}}. \quad (42)$$

This expression also applies when calculating the decay from a ND state.

Having determined the total decay width from Eq. (33), an actual decay time is selected randomly from an exponential decay function with mean decay time:

$$\tau = \frac{\hbar}{\Gamma(\text{total})}. \quad (43)$$

The actual decay channel is selected according to the probability distribution

$$p(i) = \frac{p_x(i)\Gamma(i)}{\sum_1^8 p_x(i)\Gamma(i)}, \quad (44)$$

where

$$p_x(i) = p_1, \quad i = 1, 2, 3, 4 \quad (45)$$
$$p_x(i) = p_2, \quad i = 5, 6, 7, 8. \quad (46)$$

If the selected decay channel number is less than or equal to 4, the decay took place in the ND well. If the decay channel number is 5 or higher, the nucleus decayed to a SD state. For the selected channel, the γ emission energy is selected using the γ spectral distribution for this channel, calculated using Eq. (17) or Eq. (22), depending on whether the decay was statistical ($E1$) or collective ($E2$) in character.

Starting from the entry point, the above procedure is repeated until the γ decays lead to an energy location that is under the cascades cutoff energy, U_0, for the well in which it occurs. The cutoff energy can be different in the two wells and is of the order of 1–2 MeV. At present, the last decays into the states on or near the ND and SD yrast lines, some of which give rise to discrete γ transitions, are not included in the MC calculations, as they occur in a region of low level density where a statistical treatment is no longer appropriate. However, as will be shown in Sec. VIII, it is possible to experimentally extract these γ rays associated with the last steps (dominated by the $M1/E2$ QC component) from the QC spectra (see Figs. 2 and 26).

H. Monte Carlo calculations with average rotational damping width parameters (MC1)

In a first attempt to use the MC simulations (MC1) to reproduce the measured QC and ridge spectra, the rotational damping parameters Γ_μ, $\Gamma_{rot}^{(2)}$ and the fraction of narrow to wide selection, I_{nar}, were kept constant with respect to spin and excitation energy above the yrast lines. In Sec. VII, other, possibly more realistic, functions suggested by theory [15] for the rotational damping parameters, will be considered. However, using simple average values first simplifies the calculations and, furthermore, provides a baseline for the values of the rotational damping parameters, without much theoretical bias. In addition, it is interesting to simply probe

TABLE III. (Fixed) rotational damping parameter values used in MC1 simulations to reproduce the experimentally extracted ridge and QC spectra of Figs. 5–8. These values represent *average* values in the relevant spin and excitation energy regions. Γ_μ and $\Gamma_{rot}^{(2)}$, which are HWHM measures, are related to Γ_{nar} and Γ_{wid} as shown [24,29].

Parameter	ND well, DO	ND well, Feed	SD well, Feed
$\Gamma_\mu \sim \frac{1}{2}\Gamma_{nar}$		$\sim$25 keV	$\sim$5 keV
$\Gamma_{rot}^{(2)} \sim \frac{1}{2}\Gamma_{wid}$	125 keV	240 keV	240 keV
I_{nar}	0%	17%	36%

how well the QC and ridge spectra can be reproduced with fixed rotational damping values.

Using fixed values is tantamount to ignoring such effects as (i) motional narrowing [15], the effect that reduces $\Gamma_{rot}^{(2)}$ at higher excitation energies, and (ii) the spin dependence of $\Gamma_{rot}^{(2)}$. Preliminary results of these MC1 calculations were presented in Ref. [95], before a measured entry distribution was available and the barrier height and ND yrast line (among other parameters) had been properly adjusted.

The Γ_μ, $\Gamma_{rot}^{(2)}$, and I_{nar} values in the ND and SD wells (a total of six parameters) were varied over a wide range until all the spectra of Figs. 5–8 were reproduced. Table III gives the best values of the parameters obtained in the MC1 calculations.

For the SD QC spectrum, the MC code was also used to calculate the DO spectrum. It was necessary to introduce a back-shift Δ [see Eq. (9)] of about 1.5 MeV in the MC calculations to restrict the γ-decay phase space. This was done to reproduce the overall SD QC spectrum of Fig. 5; i.e., the MC calculation suggests that in the region in spin of $\sim$20–29$\hbar$, where the DO from the SD band occurs, pairing in the ND well is not yet quenched significantly. As expected, there was no need to consider introducing any pairing in the $\sim$42–66$\hbar$ spin region where the feeding occurs. These observations are in qualitative agreement with the calculations in Ref. [76].

For the calculations describing the DO of the SD band toward the ND levels, I_{nar} is set to zero in the ND well. The ridges cannot be extracted in this spin region. Here, the $E2$ γ-ray energies are so low that too many strong discrete transitions are present in the associated region of the γ-γ matrices. As a result, the associated ridges are obscured, and it is not possible to extract the rotational damping parameters with any confidence.

In the MC calculations describing the DO of the SD band, it was also found to be necessary to reduce the value of $\Gamma_{rot}^{(2)}$ in the ND well compared with the value used in the feeding region (see Table III) in order to reproduce the SD QC spectra. Thus, the simple MC1 simulations with fixed values of the parameters indicate that over a large spin range, from the SD feeding region to the DO of the SD band, $\Gamma_{rot}^{(2)}$ in the ND well does in fact vary. As can be seen from Table III, the SD narrow rotational damping width is very small. The wide rotational damping widths, especially in the ND well, are more in line with what might be expected [15].

It is remarkable that the overall features in the spectra of Figs. 5–8 can be reproduced so well in the MC1 calculations with the simple assumption of (at least locally) constant rotational damping parameters in the SD feeding region and the DO region. However, some features are missed, such as the high-energy tail, from $\sim$1.8 to $\sim$2.7 MeV, of the ND QC spectrum in Fig. 8.

I. Monte Carlo calculations with rotational damping width functions (MC2)

As stated earlier, theory suggests that Γ_μ, $\Gamma_{rot}^{(2)}$, and I_{nar} are functions of spin and, especially, excitation energy. Below is an account of calculations, labeled MC2, which incorporate more evolved descriptions of these damping widths.

According to Ref. [15], the narrow rotational damping width $\Gamma_\mu(U)$ depends on the mass and the excitation energy above the yrast line U as

$$\Gamma_\mu(U) \sim 0.039 \left(\frac{A}{160}\right)^{-\frac{3}{2}} U^{\frac{3}{2}}, \tag{47}$$

where U and $\Gamma_\mu(U)$ are in units of MeV and $\Gamma_\mu(U)$ is a HWHM measure. Thus, according to Ref. [15], $\Gamma_\mu(U)$ does not depend on the spin or on the deformation of the nucleus. On the other hand, the wide rotational damping width depends on $\Gamma_\mu(U)$ as well as on the deformation, $\delta = 0.946 \times \beta_2$, and the spin I of the nucleus. With the following two limits defined as

$$l_1 = 0.7 \left(\frac{A}{160}\right)^{-\frac{3}{2}}, \tag{48}$$

$$l_2 = 1.5 \frac{I}{40} \left(\frac{A}{160}\right)^{-\frac{3}{2}} \left(\frac{\delta}{0.3}\right)^{-\frac{2}{3}}, \tag{49}$$

the wide rotational damping width $\Gamma_{rot}^{(2)}$ is approximately [15]

$$
\begin{aligned}
&\Gamma_{rot}^{(2)} \sim \\
&U < l_1: \qquad\qquad 0, \\
&l_1 < U < l_2: \; 0.13 \frac{I}{40} \left(\frac{A}{160}\right)^{-\frac{5}{2}} \left(\frac{\delta}{0.3}\right)^{-\frac{2}{3}} U^{\frac{1}{4}}, \\
&U > l_2: \; 0.22 \left(\frac{I}{40}\right)^2 \left(\frac{A}{160}\right)^{-\frac{13}{3}} \left(\frac{\delta}{0.3}\right)^{-2} U^{-1} \\
&\qquad\quad + 0.00044 \left(\frac{A}{160}\right)^{-\frac{5}{2}} \left(\frac{\delta}{0.3}\right)^{-2} U^{\frac{3}{2}}.
\end{aligned}
\tag{50}
$$

In the present MC calculations, interpolations are used near the boundaries l_1 and l_2 in order to produce a smooth realistic distribution of $\Gamma_{rot}^{(2)}$ as a function of I and U. The parameter l_1 defines the onset of rotational damping, which in this treatment does not depend on the deformation of the nucleus. In reality, l_1 depends on the level density. Thus, because the level density is lower in the SD well, l_1 might be somewhat higher in the SD well [23]. The parameter l_2 indicates where motional narrowing starts to dominate the rotational damping.

Lastly, the functional form of the relative intensity of the narrow rotational damping width component is taken from

Refs. [24,27]:

$$I_{\mathrm{nar}}(U) \sim \frac{1}{\rho_I(U)\Gamma_\mu(U)}, \qquad (51)$$

where ρ is the level density given in Eq. (9). Clearly, the narrow rotational damping width component should only be observed at rather low excitation energies, considering the strong dependence on U in the $\rho_I(U)$ and $\Gamma_\mu(U)$ functions [see in Eqs. (9) and (47)]. It should be noted that Eq. (51) is only valid below the energy region where motional narrowing sets in.

When the rotational damping widths and narrow fractions given by Eqs. (47), (50), and (51) were used directly in the MC calculations, i.e., not scaled or modified, it was found that the experimentally observed QC and ridge spectra could not be reproduced. Thus, in these MC2 calculations, the approach chosen consisted in (i) accepting the functional forms of the damping widths and narrow fraction of Eqs. (47), (50), and (51), but (ii) *renormalizing (scale)* these functions until the best simultaneous fits of the experimental spectra of Figs. 15–18 were achieved.

The narrow rotational damping width in the SD well is determined by the observed width of the narrow ridge in
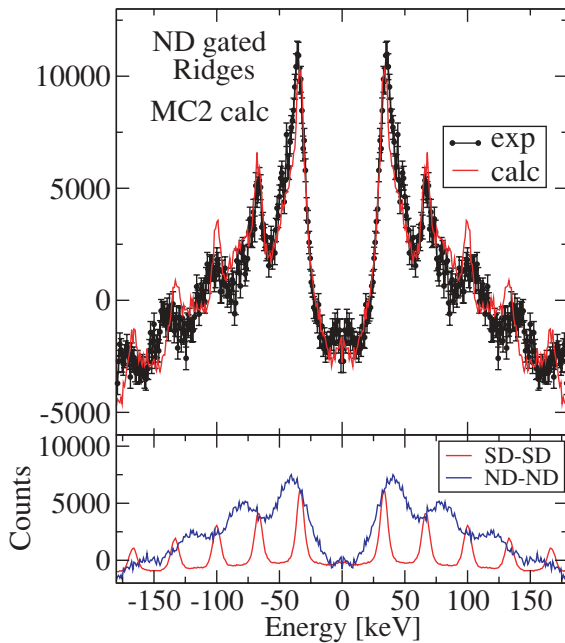

FIG. 15. (Color) Upper panel: comparison of experimentally extracted ND/ALL ridges with the best MC2 calculation using functions of the rotational damping parameters Γ_μ, $\Gamma_{\mathrm{rot}}^{(2)}$, and I_{nar} given by Eqs. (47), (50), and (51). The distributions have been multiplied by the renormalization factors given in Table IV. The ridge represents a cut of 1358 ± 212 keV along the diagonal in the $E_{\gamma 1} \times E_{\gamma 2}$ matrix. Same data as in Fig. 6, but here the statistical errors from the experimental extraction of the ridge are indicated with error bars. Lower panel: calculated ridges from γ rays emitted exclusively in either the ND or SD well. Mixed emissions are not shown, but are included in the total calculated ridge in the upper panel. It is clear that the sharpest features of the experimental ridges originate from γ rays emitted while the nucleus is in the SD well.
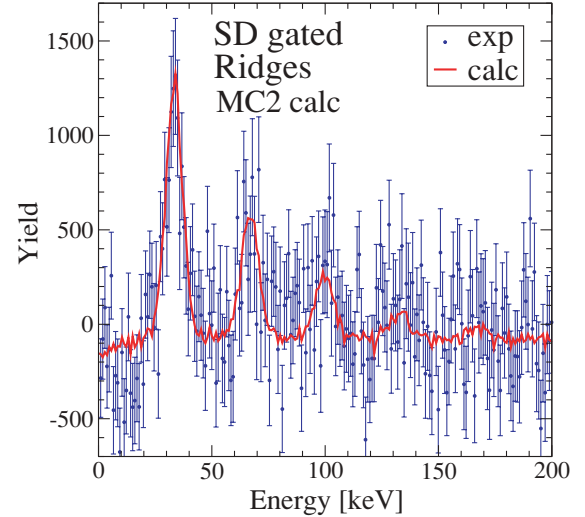

FIG. 16. (Color) Experimentally extracted SD ridges with the MC2 calculation using the Γ_μ, $\Gamma_{\mathrm{rot}}^{(2)}$, and I_{nar} functions given by Eqs. (47), (50), and (51) for both the ND and SD wells. The distributions have been multiplied by the renormalization factors given in Table IV. The ridge represents a cut of 1450 ± 350 keV along the diagonal in the $E_{\gamma 1} \times E_{\gamma 2}$ matrix. Same data as in Fig. 7. However, now only half the (symmetric) spectrum is shown, and the propagated statistical errors in the experimental extraction of the ridges are indicated by error bars.

Fig. 16. However, it should be noted that this damping width is slightly narrower than the HWHM observed in the data, since the distribution in moments of inertia also adds to the experimental width. The wide rotational damping width in the SD well is determined mostly by comparison with the broad component in the data (Fig. 16).

The fraction of selected narrow rotational damping width in the SD well can, in principle, be determined from the spectrum of Fig. 16. However, because the wide rotational damping width produces a rather flat component, the narrow fraction is not determined well from the SD ridges of Fig. 16 alone. Fortunately, the ND ridges, associated with γ rays emitted in the ND well as well as in the SD well, are a smoothly varying spectrum, and the sharp ridges in Fig. 15 depend on the narrow fraction in the SD well. Thus, the SD I_{nar} renormalization factor in Table IV is determined by reproducing both SD and

TABLE IV. To reproduce the ND and SD QC spectra and ridges of Figs. 15–18 in the MC2 calculations, it was necessary to multiply the rotational damping widths and narrow fractions given by Eqs. (47), (50), and (51) by the factors shown in this table. The resulting mean values of the distributions of Γ_μ, $\Gamma_{\mathrm{rot}}^{(2)}$, and I_{nar} presented in Figs. 19–21 are also provided. See text for further details.

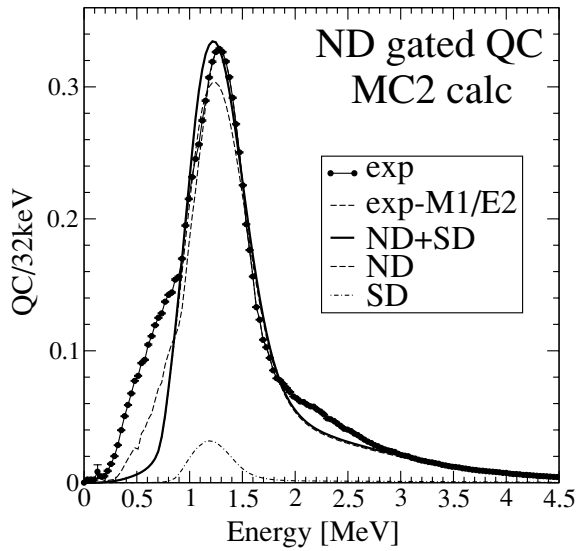| Quantity	Eq.	ND factor	ND mean value	SD factor	SD mean value
Γ_μ	(47)	0.22	21 keV	0.06	4.6 keV
$\Gamma_{\mathrm{rot}}^{(2)}$	(50)	0.55	208 keV	3.5	238 keV
I_{nar}	(51)	26	16%	3.2	35%

FIG. 17. Same as Fig. 8, but with the calculated QC spectra from the MC2 simulation where the (renormalized) functions of Γ_μ, $\Gamma_{\rm rot}^{(2)}$, and $I_{\rm nar}$ given in Eqs. (47), (50), and (51) are used rather than fixed rotational damping values.

ND ridges simultaneously. Even though the ridge spectrum in this figure appears to have a rather flat background under the sharp ridges, the value of the wide rotational damping width is by no means zero, nor is the narrow fraction in the SD well 100%. The wide rotational damping width is simply so large that the wide rotational damping component under the sharp narrow ridges *appears* to be nearly flat after the COR subtraction.

The rotational damping width parameters needed to reproduce the ND/ALL ridges in Fig. 15 are a challenge to determine, because the MC calculations suggest that about 7% of the $E2$ γ-ray emission occurs while the nucleus is in fact in the SD well. This occurs despite the fact that only a small fraction ($\sim$1%) of the γ cascades eventually get trapped
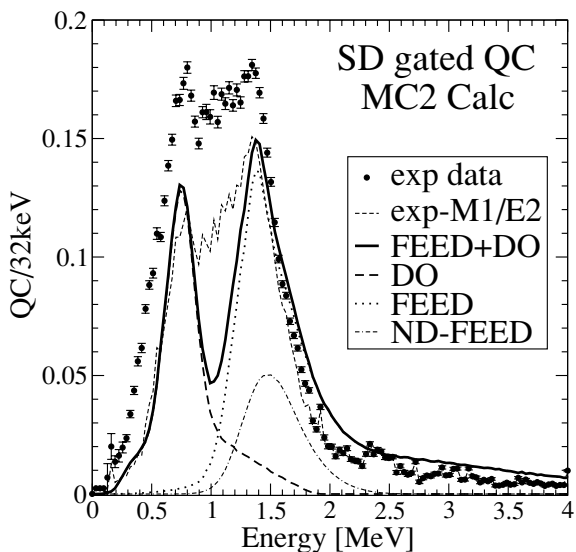
in the SD well. Consequently, as discussed above, the sharp parts of the experimental ridges seen in Fig. 15 (upper panel) are associated with the SD well and are superimposed on those associated with the ND well. This is illustrated in the lower panel of Fig. 15. Here only γ rays emitted exclusively in the ND or SD wells in the MC2 calculation are used to extract the associated ridges.

In Fig. 18, the spectrum labeled ND-FEED is from QC γ rays emitted while the nucleus resides in the ND well. Comparing this spectrum to the TOTAL spectrum reveals that $\sim$33% of the γ rays that form the SD feeding QC and SD ridge spectra are emitted while the nucleus resides in the ND well.

Thus, the rotational damping parameters in the ND and SD wells are effectively correlated in the fits to the ND and SD QC and ridge spectra. Ultimately, it proved necessary to vary *all* the renormalization factors in Table IV independently in order to find a combination that *simultaneously* reproduces the ND and SD ridges of Figs. 15 and 16 properly as well as the ND and SD QC spectra of Figs. 17 and 18. Slight adjustments of other parameters, such as the ND moment of inertia, were also required. All in all, the six renormalization factors in Table IV represent a reasonable set that reproduces, simultaneously, both the ridge and QC spectra in the ND and SD wells using the rotational damping functions determined by Eqs. (47), (50), and (51). Figures 19–21 show the distribution of the rotational damping parameters in the ND and SD wells under different gating conditions.

In the MC2 calculations with the rotational damping functions, the reductions of the $\Gamma_{\rm rot}^{(2)}$ values in the region where the SD band decays out occur naturally from the spin dependence in Eq. (50). Therefore, no special scaling of $\Gamma_{\rm rot}^{(2)}$ was necessary in this type of simulation to reproduce the QC γ rays associated with the decay of the SD band. Moreover, in

FIG. 18. Same as Fig. 5, but for the MC2 calculation.

FIG. 19. Distributions of the narrow and wide rotational damping widths, Γ_μ and $\Gamma_{\rm rot}^{(2)}$, sampled by the γ cascades in the ND well when coincidence gates are placed on clean combination of discrete ND lines. A and B mark the associated values obtained in the MC1 calculations with average rotational damping parameters (see Table III).
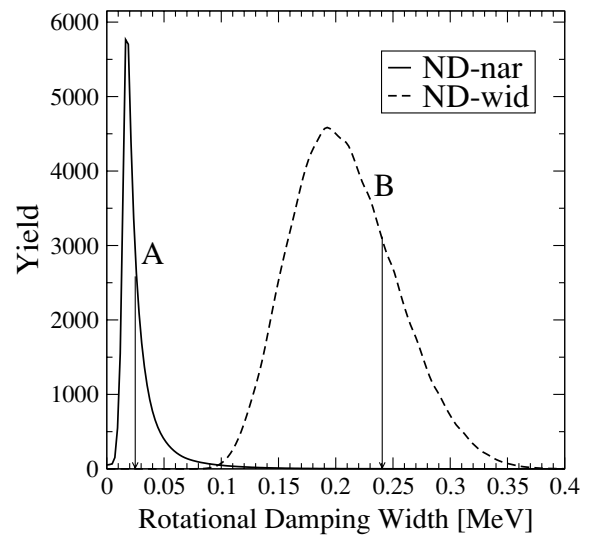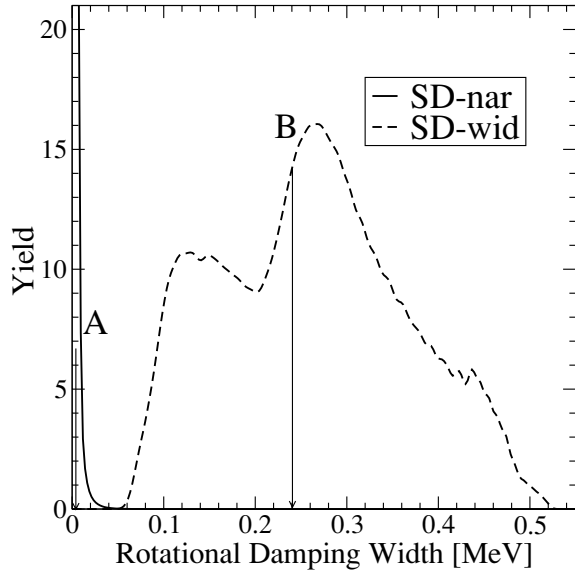
FIG. 20. Distributions of the narrow and wide rotational damping widths, Γ_μ and $\Gamma_{rot}^{(2)}$, sampled by the γ cascades in the SD well when coincidence gates are placed on clean combinations of discrete SD lines. The narrow fraction has been down scaled by a factor of 5 with respect to the wide components distribution.

contrast with the MC1 calculation, there was also no need to set Γ_μ and I_{nar} to zero in the region where the SD band decays out. The mean values of the rotational damping parameters in the DO region were found to be $\Gamma_\mu = 30$ keV and $\Gamma_{rot}^{(2)} = 72$ keV, and the narrow fraction was 15%. However, just as in the first MC1 calculation, it was necessary to introduce a back shift of about 1.8 MeV in the level density parameter formula [Eq. (9)] in this DO region in order to reproduce the combined feeding and decay QC spectrum (Fig. 18).
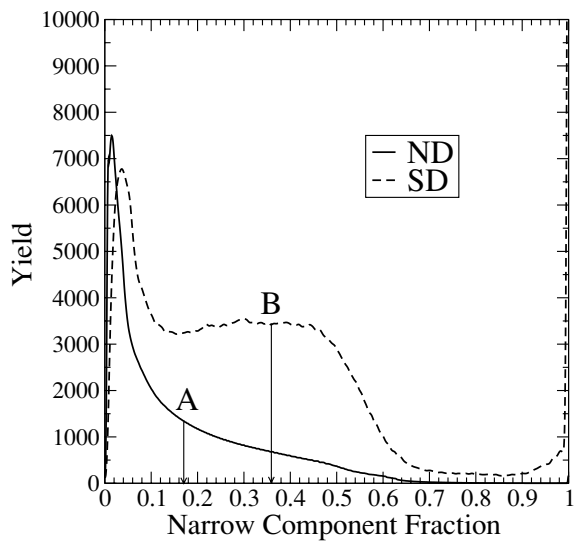

FIG. 21. Distributions of the narrow to wide rotational damping width fractions in the ND and SD wells. The 'A' and 'B' symbols mark the values obtained in the MC1 calculations with the average rotational damping parameters of Table III.

TABLE V. Miscellaneous input and output parameters associated with the MC calculations ($1\ e^2\ b^2 = 100\ e^2\ fm^2$). See text for a detailed description.

Quantity	ND, DO	ND, feed	SD, feed
	MC1 and MC2		
$\Im^{(1)}\ (\hbar^2/MeV)$	71	71	85
$\sigma\Im\ (\hbar^2/MeV)$	3.0	2.0	1.4
Δ (MeV)	1.8	0	0
$Q\ (e^2\ fm^2)$	700	700	1900
$\Im_r\ (\hbar^2/MeV)$	62.3	62.3	70.0
	MC1 Calculations		
U_0 (MeV)	3.15	1.53	1.77
Mean exit U (MeV)	$2.7 = 0.9 + \Delta$	1.0	1.0
SD feeding			3.7%
Exit time (fs)		101	13
	MC2 Calculations		
U_0 (MeV)	3.15	1.52	1.45
Mean exit U (MeV)	$2.7 = 0.9 + \Delta$	0.9	0.8
SD feeding			2.8%
Exit time (fs)		128	13

Table V provides some of the other input parameters of the MC calculations, along with miscellaneous output results. The parameter $\Im^{(1)}$ is the static moment of inertia, which for the SD band is adjusted to fit the narrow ridges in Figs. 7 and 16. For the ND well, $\Im^{(1)}$ is adjusted to fit the high-energy edge of the $E2$ component in Fig. 8 and 17, since the ND ridges shown in Figs. 6 and 15 are, to a large degree, obscured by the ridges associated with the SD well. The moments of inertia are given random Gaussian deviations around the mean $\Im^{(1)}$ values with the σ values given in Table V. Since both $\sigma\Im^{(1)}$ and Γ_μ affect the width of the narrow ridge, they may be correlated, even though they are treated as independent parameters in the MC calculations presented here. In Table V, the parameter Δ is the back shift in Eq. (9), and Q is the quadrupole moment used in the calculations [11,12,96], see Eq. (19). The parameter $\Im_r$ refers to the rigid moment of inertia used in Eq. (9). When a γ cascade decays into a state below U_0 MeV above the yrast line, the deexcitation process is stopped. The mean exit energy (above the yrast line) at which this actually occurs (which has to be less than U_0) is given next in the table. The fraction of the cascades trapped in the SD well in the MC calculations is provided along with the associated mean exit spin and decay times. In the MC calculations, successful trapping in the SD well at lower spins seems to require that the last transition of the γ cascade be a high-energy $E1$ transition in the SD well. In this spin and excitation energy region, $E2$ transitions are more probable.

J. Cross-diagonal cuts at different E_γ energies

More insight into the ridges can be obtained from cross-diagonal cuts in the $E_{\gamma 1} \times E_{\gamma 2}$ matrices at different energies. A number of such cuts are presented in Figs. 22 and 23 for the ND- and SD-gated matrices, respectively. All the cuts are made from the central energies shown in the plots, ± 107 keV along the diagonal.
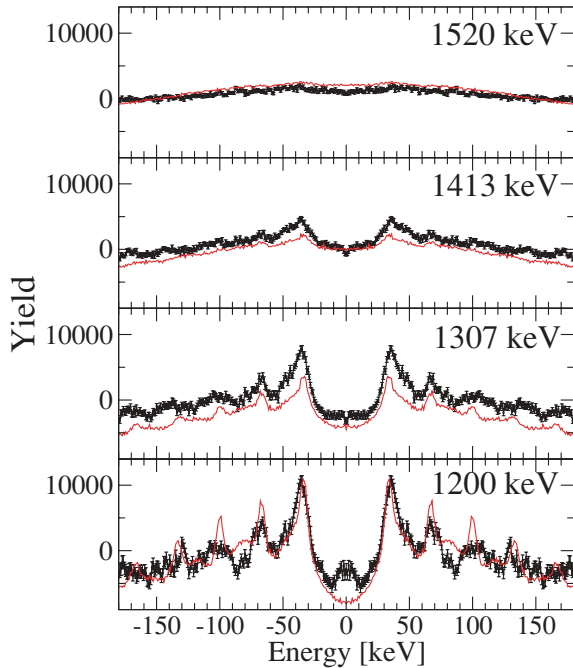
FIG. 22. (Color) Ridge spectra from the ND gated $E_{\gamma 1} \times E_{\gamma 2}$ matrix. All cuts are ±107 keV around the central energies indicated. Both the data and the MC2 calculations are shown for each cut. The results from the MC2 calculations are shown with the same offset and scaling used to reproduce the wide data cut shown in Fig. 16.

The low-energy cuts exhibit the most structure by far. As the cut energy is increased, the mean $E2$ γ-ray energy increases, and the ridges are clearly attenuated. It should be noted that the experimental low-energy cuts are, in general, more uncertain than the higher energy ones. Discrete peaks are more prominent here and introduce uncertainties in the
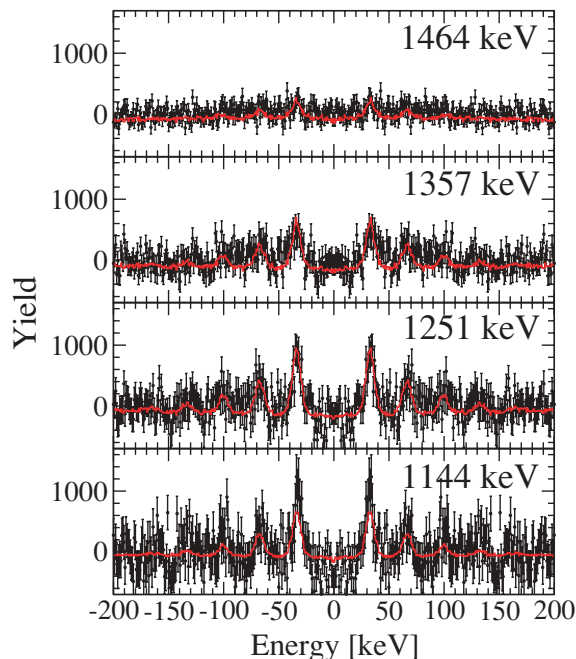

FIG. 23. (Color) Same as Fig. 22, but for the SD ridges.

experimental extraction of the ridges (see Sec. V). On the other hand, the statistics are typically better at low energy.

The MC2 calculations (presented in Figs. 15 and 16) were performed with fits to *wide* cross-diagonal cuts in the $E_{\gamma 1} \times E_{\gamma 2}$ ND and SD matrices. The cuts were 1358 ± 212 and 1450 ± 350 keV, respectively. In this way, the rotational damping parameters, in the whole region of the spin and energy plane that the QC γ cascades traverse, are probed and extracted.

Figures 22 and 23 show how the ridges from the MC2 calculation compare with the cuts made in the experimental matrices. The agreement between the experimental data and the MC2 calculations for the SD-ridge cuts is remarkably good. For the ND ridges, the overall trend of the MC2 calculation follows the data well, but the offsets are not always perfect, because the experimental and calculation COR backgrounds are not completely identical. The slightly different offsets are exacerbated by the fact that one common COR background region is used for all the slices in Figs. 22 and 23 rather than more appropriate local regions for each slice.

The moment of inertia for the SD ridges, corresponding to the cuts shown in Fig. 23, are presented in Fig. 24, where they are compared with the $\Im^{(1)}$ and $\Im^{(2)}$ moments of inertia for the discrete SD band 1. Only the narrow SD ridges are used to evaluate the $\Im^{(2)}$ moment of inertia for the SD ridges. These $\Im^{(2)}$ values are slightly larger (by ~3%) than those of the SD band 1.

VIII. DECOMPOSITION OF THE SUPERDEFORMED TOTAL SPECTRUM

The SD total spectrum was extracted in the same manner as discussed in Sec. IV. The associated QC spectrum portion can be found in Figs. 5 and 18. The *experimental* decomposition of the latter spectrum is impeded by the fact that the contribution from the DO of the SD well cannot be extracted independently
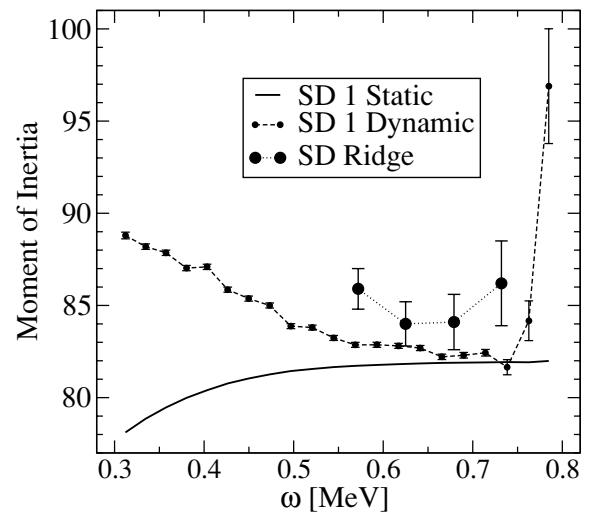

FIG. 24. Plot of the $\Im^{(1)}$ (static) and $\Im^{(2)}$ (dynamic) moments of inertia (in units of $\hbar^2$/MeV) for SD band 1 and $\Im^{(2)}$ for the SD ridges. ω is the rotational frequency, which is equal to $E_\gamma /2$.

from the feeding QC spectrum, as it was possible in the mass $\sim$190 region [9]. As shown in either of the two figures, both MC calculations clearly indicate that the feeding and decay components overlap too much to be fully disentangled.

An approximate total statistical feeding and DO component spectrum can be determined by adding (i) the calculated DO statistical component at lower energies to (ii) the feeding statistical component at higher energies. The latter was determined from the spectrum of Fig. 5 using a fit with the functional form given in Eq. (4) for energies $\geqslant$2 MeV (the fit indicates that $N = 3.1$ and $T = 0.52$ MeV). Subtracting this total statistical component from the QC spectrum does allow for the decomposition of the remaining stretched $E2$ and $M1/E2$ dipole components of the resulting spectrum through an angular distribution (A_2/A_0) analysis, just as it was carried out for the ND QC spectrum (Fig. 25). Within this approximation, the multiplicities and mean energies of the statistical, $E2$ and $M1/E2$ components of the SD QC spectrum (both from the feeding and DO of SD band 1) were determined. They are presented in Fig. 26, and the relevant information is also tabulated in Table VI. This table further provides the energy and spin removed by the discrete lines in the total spectrum of Fig. 4 and accounts for the effect of isomer tagging (marked "isomer") and coincidence gating ("missed/g").

The discrete SD lines dominate the total spin and excitation energy removed by γ rays after the last particle has been evaporated. Thus, the approximations made to experimentally extract the QC spectral components do not add significant uncertainty to the determination of the mean entry point for γ cascades feeding the SD band (Table VI). Compared with
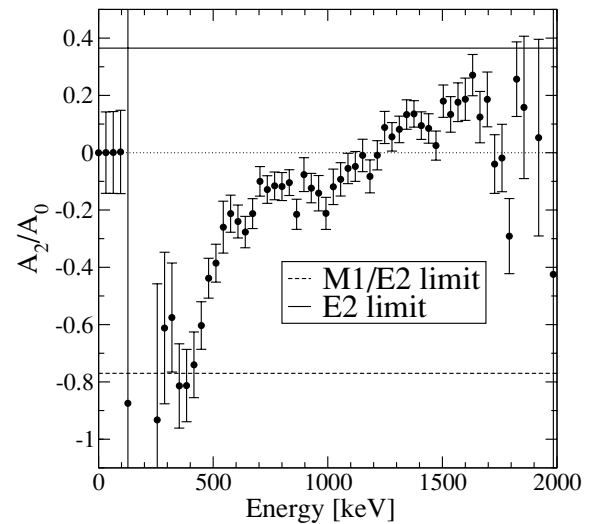

FIG. 25. Angular distribution coefficient A_2/A_0 [see Eq. (3)] for the QC spectrum of Fig. 5 *after* the approximate statistical component has been subtracted as described in the text.

the ND QC spectrum analysis in Table II, it is clear that SD band 1 is fed at significantly higher spins and relatively lower excitation energies (with respect to the yrast lines) than those of γ cascades that are *not* trapped in the SD well. This will become even more evident when the entire SD entry distribution is extracted, as described in the next section.

TABLE VI. Decomposition of all the components of the normalized QC spectrum obtained when double coincidence gates are placed on SD lines in ^{152}Dy. To arrive at the mean entry point, the contributions due to the isomer and to the lines missed because of coincidence gating are added. The last three rows provide the mean entry points from the HK analysis (see Sec. VI) and from the two MC simulations. The error estimates contain contributions from statistical uncertainties as well as systematic contributions from the background subtraction and the unfolding and normalization procedures.

Component	Multiplicity M	$\langle E \rangle$ (MeV)	$\delta I/M(\hbar)$	$\Delta I(\hbar)$	ΔE (MeV)
QC:stat	1.7(1)	1.82(1)	0.6(1)[a]	1.0(3)	3.0(2)
QC:E2	2.8(2)	1.14(1)	2.00	5.6(3)	3.2(2)
QC:$M1/E2$	1.9(2)	0.90(3)	0.5(1)[a]	0.9(2)	1.7(2)
SD disc.	12.5(7)			24.8(1.4)	12.6(7)
a/14 ns	0.9(1)			1.9(1)	0.62(5)
b/14 ns	0.87(6)			1.1(2)	0.29(3)
Unassigned	0.82(6)		1.4(2)[b]	1.2(2)	0.50(5)
Grass	1.05(6)	0.83(1)	1.4(2)[b]	1.5(2)	0.87(5)
Missed/g	2.00	0.96(1)	2.00	4.00	1.92(2)
Isomer				17.0	5.088
QC				58.8(1.5)	29.8(8)
HK				56.5(1.5)	29.1(8)
MC1				55.6	30.2
MC2				55.9	30.2

[a]Estimates based on MC2 calculations.

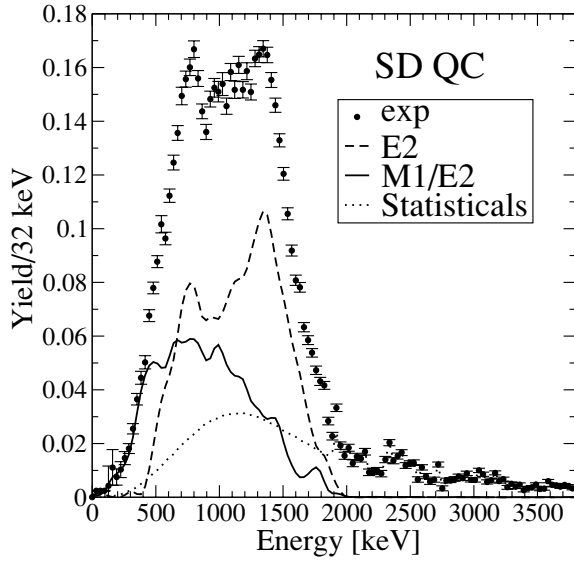[b]Assumed to be the same as for the known lines in the ND analysis.

FIG. 26. Experimental decomposition of the SD QC spectrum into the statistical $E1$, quadrupole $E2$, and $M1/E2$ components (see text for details). Components contain both the feeding and the DO γ rays associated with SD band 1 in ^{152}Dy.

IX. THE SUPERDEFORMED ENTRY DISTRIBUTION

The entry distribution for γ cascades feeding SD band 1 in ^{152}Dy was measured in the same way as for the ND states. The measured (H, K) distribution, obtained with clean double coincidence gates placed on discrete SD transitions, was unfolded as described in Sec. VI C. The mean number of Ge-BGO modules hit was determined to be 19.8(6) [23.3(8) unfolded] and, on average, 18.7(6) MeV of energy [24.0(8) unfolded] was detected.

The multiplicity must be translated to spin in order to find the SD entry distribution. The mean spin removed by the *observed* γ rays for cascades trapped in the SD well can be determined by inspecting Table VI. On average, 41.8(1.5)$\hbar$ of angular momentum is carried away by the 24.5(7) γ rays observed in GS, when SD band 1 is populated. This excludes γ rays emitted below the 17^+ isomer due to the tagging procedure. Therefore, the mean spin removed by each γ ray is 1.70(8)$\hbar$. Because longer cascades of stretched $E2$ transitions are involved, the mean $\delta I/M$ value is significantly larger than for the equivalent γ cascades that end up in the ND well [1.45(3)$\hbar$, see Sec. VI D]. The SD (I, E) entry distribution was obtained from the unfolded (M, E) distribution using the translation in Eqs. (5) and (6), but now with a coefficient of 1.70 in front of the multiplicity M. The resulting SD (I, E) entry distribution is found in Fig. 27. Obviously, the part of the entry distribution below the lowest of the two yrast lines is unphysical and attributed to uncertainties in the measurement and detector resolution. The mean entry spin and energy are 56.5(1.5)$\hbar$ and 29.1(8) MeV, which compares well with the mean values obtained from the QC spectrum analysis presented in Table VI. Compared to the ND (I, E) entry distribution of Fig. 13, the SD entry distribution has clearly moved toward higher spins and lower excitation energies with respect to the yrast lines (heat energy U).
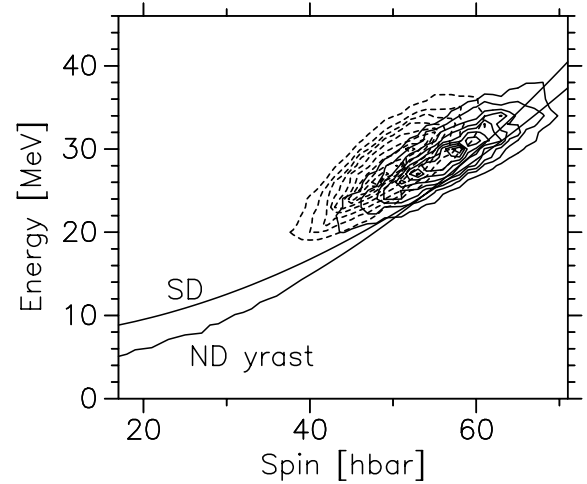

FIG. 27. Contour plots of the measured normal deformed (dashed) and superdeformed (solid) entry distributions. The normal deformed and superdeformed yrast lines used in the Monte Carlo calculations are shown as well. The mean entry spins and energies are [49.5(1.0)$\hbar$, 28.0(6) MeV] and [56.5(1.5)$\hbar$, 29.1(8) MeV] for the normal deformed and superdeformed distributions, respectively. Thus, the superdeformed distribution is higher by 7.0(1.8)$\hbar$ in spin, but only 1.1(1.0) MeV in energy, with respect to the normal deformed entry distribution.

The SD entry distribution can also be extracted from the MC2 calculation by binning the entry points of the γ cascades trapped successfully in the SD well. This entry distribution exhibits the same behavior as the experimentally extracted one (Fig. 27), with a mean spin of $\sim$56$\hbar$ and an excitation energy of $\sim$30 MeV. This is also in good agreement with (i) the mean entry point determined from the total SD γ spectrum and (ii) the mean of the measured SD entry distribution as shown in Table II. This demonstrates that the MC model calculations also reproduce the special selection of entry points of Fig. 27 leading to the population of SD band 1.

The maximum angular momentum that can be transferred to the compound nucleus in a heavy-ion fusion reaction is roughly given by [55,97,98]

$$L_{\max}[\hbar] = 0.219 \times (R_{CB}[\text{fm}] + R_t[\text{fm}]) \tag{52}$$
$$\times \sqrt{\mu(E_{CMS}[\text{MeV}] - E_{CB}[\text{MeV}])}, \tag{53}$$

where

$$R_{CB} = 1.2\left(A_1^{\frac{1}{3}} + A_2^{\frac{1}{3}}\right)[\text{fm}], \tag{54}$$
$$E_{CB} = 1.44\frac{Z_1 Z_2}{R_{CB}[\text{fm}] + R_t[\text{fm}]}[\text{MeV}], \tag{55}$$
$$R_t \approx 2.0\,\text{fm}, \tag{56}$$
$$\mu = \frac{A_1 A_2}{A_1 + A_2}, \tag{57}$$
$$E_{CMS} = \frac{M_2}{M_1 + M_2}E_1. \tag{58}$$

Thus, assuming that the four neutrons evaporated in this reaction each, on average, remove $\sim$1.5$\hbar$ of spin, the maximum angular momentum imparted to the ^{152}Dy residue with the present reaction is $\sim$66$\hbar$. This value is very close to the upper

edge of the measured (I, E) entry distribution for the SD γ cascades presented in Fig. 27. The spin of the highest discrete SD state in band 1 is, incidentally, also $66\hbar$ [6]. The maximum energy transferred to the ^{152}Dy residue is $\sim$2 MeV assuming that the four neutrons each remove about 1 MeV of kinetic energy. This places an even more stringent upper limit on the energy of the entry distribution in Fig 27; i.e., SD band 1 in ^{152}Dy is indeed fed at the limits of both the spin and excitation energy provided in the heavy-ion fusion process.

X. CONCLUSIONS AND FUTURE DIRECTIONS

Well-defined ridges, resulting from γ-γ correlations at finite temperature in the cooling of ^{152}Dy by quasicontinuum γ rays, have been extracted in this work. The quasicontinuum γ rays were likewise extracted with double coincidence gates placed on clean combinations of normal deformed and superdeformed discrete lines. The entry distribution for the reaction ^{108}Pd(^{48}Ca,4n)^{152}Dy at 191 MeV (midtarget) was measured and used as a starting point for Monte Carlo simulations of these γ cascades. Through these simulations, it was possible to ascertain the strength of the rotational damping widths in the normal deformed and superdeformed wells of ^{152}Dy. Very few other measurements of the rotational damping properties in a superdeformed well in the mass $A \sim 150$ region have been made [99]. Only recently have the rotational damping properties in the superdeformed well in the mass $A \sim 190$ region been probed [38]. Finally, the superdeformed entry distribution was extracted and compared with the total entry distribution. As expected, the superdeformed band is fed at higher spins and at lower excitation energies with respect to the yrast lines than are the normal deformed bands.

All the available data, i.e., the normal deformed and superdeformed quasicontinuum and ridge spectra, can be reproduced reasonably well by the Monte Carlo simulations. Thus, the Monte Carlo model seems to contain most, if not all, the physics ingredients necessary to describe the cooling of the ^{152}Dy nucleus. This instills some confidence in the extracted values for the rotational damping width parameters in the normal deformed and superdeformed wells. Those values are summarized in Tables III and IV.

In general, the theoretical Γ_μ, $\Gamma_{\mathrm{rot}}^{(2)}$, and I_{nar} rotational damping functions must be renormalized by rather large factors (see Table IV) in order to reproduce the experimental data. This suggests that more theoretical work needs to be carried out to fully understand rotational damping. The large value of the scaling factor for the normal deformed narrow fraction damping component could be reduced significantly if a larger level density parameter a [see Eq. (9)] was used (e.g, $A/8$ or $A/9$ instead of $A/7$ MeV^{-1}). Furthermore, with the very small value of Γ_μ in the superdeformed well, it cannot be ruled out that the observed narrow ridges are from either ergodic bands [32,37] or unmixed bands.

It will be important to determine rotational damping values in other regions of the nuclear chart, using the methods described in this work, to aid in the theoretical understanding. For the ^{152}Dy superdeformed well, Matsuo *et al.* calculated values of 59 and 67 keV for Γ_μ and $\Gamma_{\mathrm{rot}}^{(2)}$, respectively [25].

These predictions are in poor agreement with the present results.

Superdeformed ridge spectra in an experiment on ^{149}Gd [99] display a narrow ridge 20 keV wide, corresponding in the present interpretation to $\Gamma_\mu \sim 10$ keV. This is only slightly larger than the small value found in this work, $\sim$5 keV. In the analysis of the same experiment, a wide width of $\Gamma_{\mathrm{rot}}^{(2)} \sim$100–150 keV was applied, together with a distribution of in-band probabilities corresponding to I_{nar} of about 30–40%. Reference [23] calculates $\Gamma_{\mathrm{rot}}^{(2)} = $ 30–70 keV in the superdeformed well, which is less than the width found in this work, $\sim$240 keV and 238 keV (see Tables III and IV).

The average of the rotational damping width values in the MC2 calculations agree well with the fixed values used in the MC1 simulations. The MC2 results reproduce the experimental data only slightly better than the MC1 calculations. Thus, another test is needed to demonstrate that the spin and excitation energy dependent rotational damping functions used in the MC2 simulations are more suitable than the simple average or fixed values employed in the MC1 approach. Populating the nucleus using the same reaction, but at different beam energies, would provide such a test. Furthermore, to better determine the rotational damping parameters in the normal deformed well, the normal deformed ridges should be measured at lower beam energies as well, since fewer γ rays would then be emitted while the ^{152}Dy nucleus resides in the superdeformed well. In this way, the normal deformed rotational damping parameters could be extracted with less "interference" than was found to be the case here. Moreover, such experiments would also probe wider regions in spin and excitation energy of the rotational damping distributions [given by Eqs. (47), (50), and (51)] than the cuts in Figs. 22 and 23 did.

It would also be interesting to investigate whether the $E2$ high-energy tail in the normal deformed quasicontinuum spectrum (Fig. 17) disappears when the beam energy is reduced, i.e., whether this feature originates from the superdeformed or normal deformed well. This high-energy tail most likely stems from γ cascades that pass through a region with a larger rotational damping width than is currently included in the Monte Carlo simulations. A delayed onset of motional narrowing, see l_1 in Eq. (50), might also help to reproduce this feature of the quasicontinuum spectrum.

Very narrow ridges have recently been found in ^{194}Hg as well [38]. Moreover, in this case, it was found that the intensity of the narrow ridges exhausts the total $E2$ decay strength. This implies that I_{nar} is nearly 100% in the superdeformed well of ^{194}Hg.

Having found that the decay-out quasicontinuum spectrum associated with the decay of the superdeformed band 1 in ^{152}Dy is quite different from the corresponding spectrum in the mass $\sim$190 region [9], work is in progress to characterize the decay-out quasicontinuum spectrum for superdeformed bands in the $A \sim 130$ region [100]. It will be interesting to see if the decay out of superdeformed bands in this mass region occurs primarily through statistical γ rays ($\sim$90%) as is the case in the mass $\sim$190 region [9] or if $E2$

transitions play a significant role, as found here in the nucleus ^{152}Dy. Indeed, the MC2 calculations suggest that about 68% of the decay-out quasicontinuum γ rays are of this $E2$ character.

APPENDIX A: EFFICIENCY OF GAMMASPHERE

The photopeak efficiency of GS can be found from a spectrum collected with a ^{60}Co [51] source placed in the center of the array [101]. If $\epsilon_p(E_\gamma)$ is the photopeak efficiency at the energy E_γ, then the counts (peak areas in associated spectrum) A in the two ^{60}Co peaks at 1173 keV, 1333 keV and their sum peak are related as

$$A(1173) = C * \epsilon_p(1173)(1 - C_o\epsilon_c(1333) * C_f), \quad \text{(A1)}$$

$$A(1333) = C * \epsilon_p(1333)(1 - C_o\epsilon_c(1173) * C_f), \quad \text{(A2)}$$

$$A(2506) = C * \epsilon_p(1173)\epsilon_p(1333) * C_f, \quad \text{(A3)}$$

$$\text{with} \quad \epsilon_T = \epsilon_p + \epsilon_c \quad \text{(A4)}$$

$$\text{and} \quad P_T = \epsilon_p/\epsilon_T, \quad \text{(A5)}$$

where ϵ_T is the total efficiency, P_T the photopeak to total ratio, and ϵ_c the Compton scattering efficiency. The factor C_f takes into account the angular correlation between the 1173 and 1333 keV γ rays striking the same detector, summing up to 2506 keV. The factor $(1 - C_o\epsilon_c() * C_f)$ corrects for the fact that one of the γ rays may Compton scatter in the same germanium detector and thus will remove counts that should belong to the photopeak of the other γ ray. If only this effect is included, $C_o \equiv 1$. Scattering of one of the two γ rays from, e.g., the nearby Hevimet shields into the germanium detector may be taken into account by setting $C_o > 1$.

It follows that the efficiency of GS at 1333 keV for 100 detectors in the array can be determined as

$$
\begin{aligned}
\epsilon_p(1333) = {} & 100 \times A(2506)/A(1173)/C_f \\
& \Big/ \left(1 + C_o \frac{A(2506)}{A(1173)} \frac{(1 - P_T(1333))}{P_T(1333)}\right). \quad \text{(A6)}
\end{aligned}
$$

For the ^{60}Co source, C_f is found to be $(1 + 0.1023 + 0.0086) = 1.1109$ [102] at $0°$. Taking into account the opening angle of the Ge detectors ($\pm 7.5°$), the effective C_f value is determined to be 1.109. The response function shows that the photopeak to total ratio, P_T, at 1333 keV is 0.50. For the first experiment, where the Hevimet shields were shielding the BGO detectors, the total photopeak efficiency was found to

be 8.9(2)% with $C_o = 1.25(25)$. It follows that the total γ-ray efficiency, ϵ_T, for GS in this experiment, with 100 detectors, was 17.8(4)% at 1333 keV. The average photopeak efficiency of the Ge detectors, measured with respect to the efficiency of a standard 3×3 NaI(TI) at 25 cm (0.0012), was 74(2)%.

The data used to determine the $\epsilon_p(1333)$ photopeak efficiency of GS was sorted so that only events with a multiplicity of one or two were accepted, eliminating many scattered events. Any events with "defects" of any kind (e.g., honeycomb suppression, a missing time signal, or low energy signal) were rejected, and the data were carefully background subtracted.

APPENDIX B: UNFOLDING

To properly extract the QC spectra, the sorted spectra must be unfolded; i.e., the scattered γ rays that are not suppressed by the BGO suppressor shields surrounding the Ge crystals must be removed (using the unfolding procedure described in Sec. III). The quality of the unfolding is critical for the present analysis; the true QC γ rays can *only* be extracted if the unsuppressed contribution from Compton events can be removed reliably.

The quality of the procedure can be ascertained by unfolding the γ-ray spectrum from a ^{152}Eu source placed in the center of the GS. Because this source has many lines, it is a good representation of a typical spectrum obtained when coincidence gates are placed on γ rays from an in-beam experiment. The ^{152}Eu source has no continuum associated with it. Thus, after proper background subtraction and unfolding, the spectrum should contain only peaks and *no* continuum. Figure 28 illustrates just how well the unfolding works when a response function is measured with great care. The response function does not change much at higher γ-ray
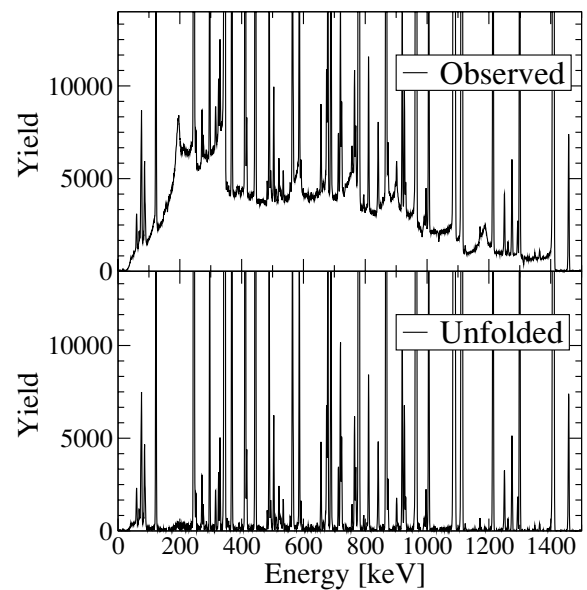

FIG. 28. γ-ray spectrum from a ^{152}Eu source as observed in GS and after it was unfolded using the response functions measured immediately after the experiment.

energies [48]. Thus, even though the highest energy at which the GS response function was measured was 1836 keV (see Table I), the unfolding of the measured spectra at high γ-ray energies is very reliable.

It has been found that the Compton suppression of the Ge detectors in GS tends to deteriorate over time as the performance of the BGO detectors deteriorates. It is, therefore, important to obtain a current response function just before or after experiments when the unfolding of 1D and 2D spectra is needed, as done in this work.

APPENDIX C: OBSERVED BAND INTENSITY

A portion of the intensity profile of SD bands, as a function of spin, is typically flat [1,2]. In this spin region, there is no longer any feeding of the band and the DO has not yet begun. To find this "plateau," it is necessary to first place (double) coincidence gates on very high spin transitions in order to determine the location within the SD cascade where the intensity profile decreases due to the DO process. Then, (double) coincidence gates must be placed on very low spin transitions to determine the upper edge of the intensity plateau in the same manner. Once the plateau portion of the intensity profile has been established, more precise low and high spin (double) coincidence gates can be placed, leaving a common set of plateau lines untouched, i.e., they are not used as gates. The high-spin and low-spin portions of the intensity profiles so measured can then be normalized on these common plateau lines to determine the *total* intensity profile for the SD band. Using this procedure, the total intensity curve was determined for SD band 1 in ^{152}Dy, as populated in the ^{108}Pd(^{48}Ca,4n)^{152}Dy reaction at 191 MeV (midtarget). The result, I^0, is given in Table VII along with the spin of the SD states [6] and the energy of the γ rays.

The intensity I^0 in Table VII gives the yield in the SD band if none of the SD band transitions are used in the process of gating. In practice, this can never be the case. The SD bands that are measured are always from the sum of spectra where a (large) number of combinations the SD transitions have been used as double coincidence gates. As a result, the intensities of the SD lines in such spectra are distorted. Likewise, the intensity profile itself is altered by the particular choice of double coincidence gates. A procedure describing how both of these effects can be calculated is given below. It will also be shown how a SD band can be normalized to the number of γ cascades forming the summed coincidence spectrum by using the intensity of the gating SD lines themselves.

For a particular coincidence gate combination (i, j) the proper relative intensity curve of the gated spectrum can be found from the I^0 values in Table VII:

For $k \leqslant P_l$, $I_{i,j}(k) = \max(1, I^0(k)/I^0(i))$.

For $k \geqslant P_h$, $I_{i,j}(k) = \max(1, I^0(k)/I^0(j))$.

Here, P_l and P_h indicate the lower and higher edges of the plateau, respectively. Only if both coincidence gates are in the plateau region will the intensity profile have the shape given in the I^0 column of Table VII. In all other cases,

the profile is different with a plateau that stretches between the gates.

The total intensity of the sum of spectra where double coincidence gates have been placed is found through the sum

$$I^G(k) = \left(\sum_{(i,j) \in Q} I_{i,j}(k) \frac{\epsilon_p(i)}{1 + \text{ICC}(i)} \times I_{i,j}(k) \frac{\epsilon_p(j)}{1 + \text{ICC}(j)} \right)$$
$$\bigg/ \left(\sum_{(i,j) \in Q} \frac{\epsilon_p(i)}{1 + \text{ICC}(i)} \times \frac{\epsilon_p(j)}{1 + \text{ICC}(j)} \right), \quad \text{(C1)}$$

where Q denotes the particular ensemble of double coincidence gates in use, in this particular case the cleanest 94 of 120 possible combinations of coincidence gates, see Sec. IV. The internal conversion coefficient is ICC, and ϵ_p is the (relative) photopeak efficiency at the energy of the gate. $I^G(k)$ is, however, not the *observed* intensity of the SD band, because the gates forming the individual profiles do not contain the gating transitions themselves, i.e., they appear in the summed spectrum only as contributions of combinations of gates that do not contain them. This gating effect can be taken into account using the same sum as in Eq. (C1), but for each (i, j) double coincidence gate intensity profile, removing the intensity of the coincidence gates i and j themselves in the $I_{i,j}(k)$ profiles. If this modified sum is called $I^{nG}(k)$, the factors that should be used to correct for the missing coincidence gates, when areas of SD lines are extracted, is simply

$$G_f = I^G(k)/I^{nG}(k). \quad \text{(C2)}$$

To find the intensity of the SD band based on the individual coincidence gates, the actual band intensity should be divided out as

$$T_f = (1 + \text{ICC}(k)) \times G_f/I^G(k)$$
$$= (1 + \text{ICC}(k))/I^{nG}(k), \quad \text{(C3)}$$

where it is assumed that the area of the SD peak, A_g, has already been extracted from a spectrum that has been corrected for (relative) efficiency, but not corrected for internal conversion (which is usually the case). The $A_g \times T_f$ product for any of the SD lines should give the same value within propagated errors, namely, the number of γ cascades that formed the spectrum (which can be used for normalization purposes).

Table VII gives the unbiased band intensities and correction factors found in the present case. Figure 29 illustrates how well the normalization works. The curve marked [oi] shows the observed intensity in the sum of double coincidence gated specta. Curve [gci] provides the intensity when a correction for the missing intensity in the coincidence gates is applied using the G_f factor, while [cbi] presents the intensity profile that was calculated for the SD band using the procedure denoted above as $I^G(k)$. The [gci] and [cbi] curves agree well with one another but, because of the effects of gating, are quite different from the unbiased intensity curve, I^0 (labeled [ub]). Finally, the line labeled [sdn] shows the $A_g \times T_f$ product which determines the number of γ cascades that formed the SD band and, thus, allows the SD band to be normalized to multiplicity, see Fig. 4. Note that the extracted areas labeled [oi], [sdn], and

TABLE VII. Spins of levels and energies of γ rays in SD band 1 of ^{152}Dy. I^0 is the unbiased intensity of the band determined as described in the text. I^G is the effective intensity of the summed coincidence spectra, where double coincidence gates have been placed on the cleanest 94 of 120 possible combinations of gates. Notice how I^G differs significantly from I^0 because of the coincidence gating. G_f and T_f factors are discussed in the text. States marked with asterisk are considered to be in the plateau region discussed in the text. Correction factors are only calculated for transitions used as gates.

Spin($\hbar$)	Energy (keV)	I^0	I^G	G_f	T_f	$F/D^0(\%)$	$F/D^G(\%)$
24						-13	-15
26	601.2	0.13				-27	-31
28	646.2	0.40	0.46	1.09	2.39	-40	-44
30	691.5	0.82	0.89	1.29	1.44	0	0
32	737.1	0.82	0.89	1.27	1.43	-18	-10
34	782.9	0.99*	0.99	1.16	1.16	-2	
36	828.9	1.02*	1.00	1.26	1.26		
38	875.5	1.01*	1.00	1.27	1.27		
40	922.3	0.99*	1.00	1.27	1.28		
42	969.5	$1.00 + 0.24^*$				$+6.8$	$+2.3$
44	1016.8	0.93	0.98	1.13	1.15	$+6.3$	$+2.0$
46	1064.4	0.87	0.95	1.17	1.23	$+6.9$	$+2.5$
48	1112.2	0.80				$+1.5$	$+2.5$
50	1160.2	0.79	0.90	1.20	1.33	$+2.7$	$+1.4$
52	1208.3	0.76	0.89	1.17	1.31	$+9.8$	$+8.3$
54	1256.5	0.66	0.81	1.16	1.43	$+13.0$	$+12.7$
56	1304.7	0.53	0.68	1.13	1.66	$+18.3$	$+20.0$
58	1353.1	0.35	0.48	1.12	2.33	$+13.6$	$+17.5$
60	1401.5	0.21	0.30	1.10	3.60	$+10.5$	$+13.7$
62	1449.7	0.11	0.17	1.10	6.61	$+5.7$	$+9.0$
64	1497.9	0.05				$+3.8$	$+6.0$
66	1544.6	0.01				$+1.1$	$+1.7$
68	1580						

[gci] were normalized to the weighted mean of all the $A_g \times T_f$ product values in Fig. 29, in order to render the plot more instructive by showing the various effects discussed above.
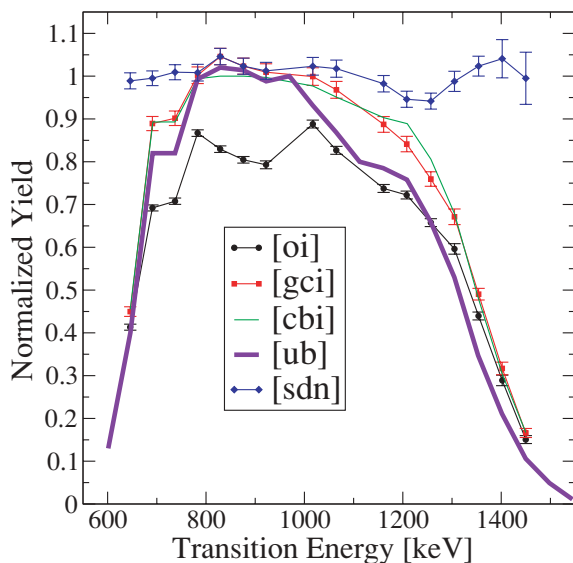

FIG. 29. (Color) Observed and modified intensities of SD band 1. See text for discussion and definition of the labels.

APPENDIX D: BIAS SPECTRUM TEST

To extract the ridges from the coincidence matrices, it is of paramount importance to remove any discrete line in the areas of the matrices from which the cross-diagonal ridges are projected. In this work, it was also found that it is *very* important to remove any strong stripes along the $E_{\gamma 1}$ and $E_{\gamma 2}$ axes in order to improve the sensitivity of the ridge extraction. A standard procedure, when just peaks are removed, consists in the use of the level scheme to determine the location of coincidence peaks in the 2D matrices and subtract them according to their intensities. However, in the particular case of ^{152}Dy, the level scheme is not known well enough to carry out this procedure thoroughly. Moreover, the removal of the stripes also requires a correction. Thus, a new, different approach is employed. The peaks and stripes are simply removed completely in the 2D matrix, and the resulting bias this causes is extracted, as discussed in Sec. V. The extracted ridges are then corrected for this introduced bias.

In this Appendix, the distortion of the extracted ridges using this new bias correction method is explored. Figure 30 presents two ridge spectra. Using the calculated SD $\gamma\gamma$ matrix as a bench mark, one spectrum is projected onto the cross diagonal in the same manner as done with the experimental data, but without any removal of peaks or stripes, which is not necessary in this case since the *calculated* $\gamma\gamma$ matrix does not contain any discrete peak. This spectrum is labeled "true"
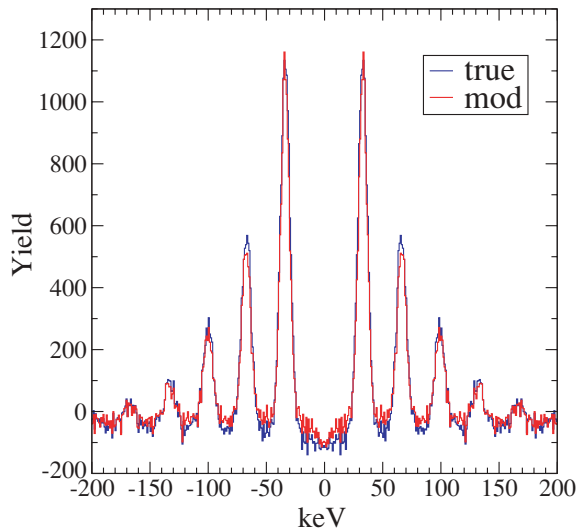
FIG. 30. (Color) Comparison of (simulated) true SD ridges with the ridges that are extracted after removing peaks and stripes from the (simulated) coincidence matrix. The bias correction has been applied in the same manner as done for the experimental data. See text for discussion.

and shows how the experimental SD ridges would appear if it was not necessary to remove peaks and stripes. The other spectrum, labeled "mod," is the same projection, but this time the SD peaks and stripes were removed (even though they are not there) before the projection, and the bias spectrum was used to correct the cross-diagonal projection accordingly. Apart from a scaling (the mod spectrum was multiplied by 1.1 before being plotted) the true and mod ridges are essentially indistinguishable. The mod spectrum has less statistics because the matrix from which the peaks and stripes have been removed obviously contains less counts.

Figure 31 presents the same test for the ND QC γ cascades. Also in this case, the mod spectrum comes quite close to the true spectrum apart from small details (most notably close to the diagonal). Nevertheless, for all comparisons of
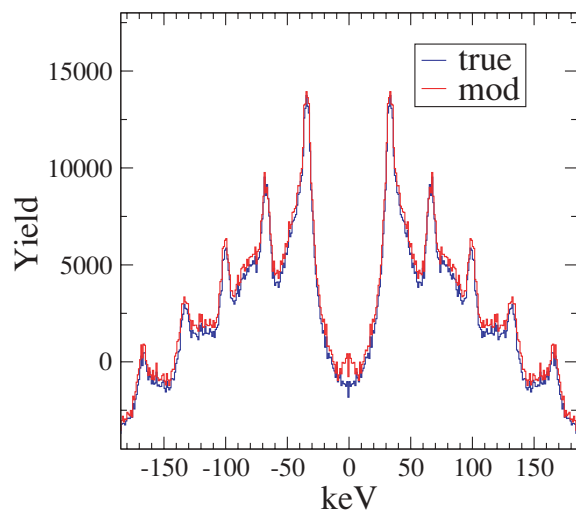

FIG. 31. (Color) Same as Fig. 30, but for the ND ridges.

TABLE VIII. Entry and exit points for the ND γ cascades. See text for details. The column marked U_{ND} (U_{SD}) indicates the heat energy above the ND (SD) yrast line.

Point	Spin ($\hbar$)	E^* energy (MeV)	U_{ND} (MeV)	U_{SD} (MeV)
(1) entry (HK)	49.5(1.0)	28.0(6)	6.8(1.0)	6.1(6)
(2) entry (QC)	49.0(1.0)	29.3(7)	8.4(7)	7.7(7)
(3) entry (MC1)	49.9	28.3	6.7	6.3
(4) entry (MC2)	49.9	28.3	6.7	6.3
(5) exit QC (MC1)	34.8	13.1	1.0	
(6) exit QC (MC2)	35.4	13.5	0.9	
(7) entry ND	$\sim$34			

experimentally extracted ridges with ridges calculated in the MC code, *both* ridges have been processed identically so that the comparison between experiment and calculations remains fair, i.e., they are affected identically by the slight distortion due to the bias correction procedure.

APPENDIX E: SELECTED MEAN VALUES IN THE NORMAL AND SUPERDEFORMED DECAY PATHS

Table VIII provides the mean entry points from (1) the 2D HK analysis and (2) the QC analysis, as well as the mean entry points (3) and (4) of the γ cascades in the two MC calculations where the γ cascades feed the ND well directly. Also shown are the mean end points (5) and (6) of these calculated γ cascades. Because the level scheme for ^{152}Dy is not yet known well enough at high spins, the experimental entry point into the ND discrete states is difficult to determine. A rough estimate, after making a number of assumptions on the spins and multipolarities of weaker γ lines in the spectrum of Fig. 1, yields an estimate of about $34\hbar$ after the isomer has been added, which is in good agreement with the values in lines (5) and (6) of Table VIII.

Table IX gives the mean feeding and decay points for SD band 1 in ^{152}Dy. The entry points in rows (1) and (2) are from

TABLE IX. Entry and exit points for the SD γ cascades. See text for details.

Point	Spin($\hbar$)	E^* energy (MeV)	U_{ND} (MeV)	U_{SD} (MeV)
(1) entry (HK)	56.5(1.5)	29.1(8)		2.3(8)
(2) entry (QC)	58.8(1.5)	29.8(8)		1.1(8)
(3) entry (MC1)	54.9	30.4		1.8
(4) entry (MC2)	55.2	30.4		1.7
(5) exit QC (MC1)	49.7	23.1		1.0
(6) exit QC (MC2)	50.0	23.2		0.8
(7) disc feed (EXP^0)	54.1			
(8) disc feed (EXP^G)	56.7			
(9) disc DO^0	27.8			
(10) disc DO^G	27.2			
(11) exit QC (MC1)	24.1	10.0	2.7	
(12) exit QC (MC2)	24.1	10.0	2.7	
(12) exp entry ND	$\sim$22			

the HK and QC analysis, respectively. Rows (3) and (4) provide the entry points for the γ cascades trapped in the SD well in the MC calculations. These entry points are different from the ND γ cascade entry points given in Table VIII in rows (3) and (4). The mean exit points for the feeding γ cascades in the MC calculations are given in rows (5) and (6). Rows (7) and (8) indicate the experimentally determined entry points into the discrete SD band 1. Row (7) does so without any gating bias, while row (8) shows the effective entry point forced up in spin by placing coincidence gates on high spin members of the SD band. It can be is seen that the MC calculations have γ cascades that are slightly longer than the values consistent with entries (7) and (8) in Table IX.

Rows (9) and (10) relate to the mean DO points for the SD band, again without and with the bias from the coincidence gates used to extract the SD band of Fig. 4. The mean end points of the QC γ cascades from the MC calculations are found in rows (11) and (12); and, finally, an estimate of the mean spin at which the SD band decays into the ND discrete states is given in row (13).

APPENDIX F: OTHER LEVEL DENSITY FORMULAS

The level density formula in Eq. (9) is not the only choice possible for use in the MC simulations of this work. Three other level density formulas are presented below. The main effect of changing to any of these other level density formulas in the MC calculations would be to force a change in the rescaling parameter for the narrow fraction rotational damping parameter, see Table IV and Eq. (51). Since Eq. (51) is derived through a cranking calculation, using expressions (F4), (F5), or (F6) below is in principle more appropriate.

The main difference between Eq. (9) and the level density formulas presented below is, besides some scaling of the level density values, the dependence on spin. Equation (F4) includes a saturation of the level density above a certain spin, whereas the formulas (F5) and (F6) have no spin dependence at all. The ND γ cascades are not affected much by this saturation since $\sqrt{(U - \Delta)/b} \sim 50\hbar$. On the other hand, in the SD well, $\sqrt{(U - \Delta)/b} \sim 40\hbar$ so the γ cascades at very high spins would be somewhat affected if Eq. (F4) was used.

Changing the level density formula in the MC calculations would have other effects, such as making the statistical spectrum slightly softer, i.e., T in Eq. (4) would decrease in value, because the $\Delta I = 1$ transitions would no longer be favored as much over the $\Delta I = 0, -1$, $E1$ transitions. As a result, the γ cascades would cool slightly less before the $E2$ γ rays were emitted.

It should be noted that the proper level density parameter a to be used in the (F4), (F5) and (F6) formulas do not *have* to be $a \sim A/7$ MeV^{-1} and $a \sim A/10$ MeV^{-1} in the ND and SD wells, respectively. In principle, those values only apply to

Eq. (9). The proper values to use in the other formulas could be obtained from information on the level density at the neutron separation energy [103] and a scaling procedure, or directly from theoretical calculations [23,33,71].

1. Åberg's level density formula

A new level density formula has been presented by Sven Åberg [75]. In his approach, three new parameters are introduced. The first is

$$b = \frac{\hbar^2}{2\Im_r^z} - \frac{\hbar^2}{2\Im_r^x}, \tag{F1}$$

where $\Im_r^z = \Im_r$ and $\Im_r^x$ are the rigid moments of inertia around the short and long axis of the nucleus, respectively [see Eq. (12)]. The second parameter is

$$I_0 = \begin{cases} I & \text{for} \quad I < \sqrt{(U - \Delta)/b}, \\ \sqrt{(U - \Delta)/b} & \text{for} \quad I > \sqrt{(U - \Delta)/b}. \end{cases} \tag{F2}$$

The final parameter is

$$c = b \times \left[\sqrt{\frac{a}{U - \Delta}} - \frac{3}{2(U - \Delta)} \right]. \tag{F3}$$

With these three parameters, the level density at high spin is evaluated as

$$\begin{aligned} \rho_I(U) = {} & \frac{1}{24} \sqrt{\frac{\hbar^2}{2\Im_r^z}} \sqrt{\frac{\pi}{c}} (U - \Delta)^{-1.5} \\ & \times e^{2\sqrt{a(U-\Delta)}} \operatorname{erf}(\sqrt{0.5c(2I_0 + 1)}). \end{aligned} \tag{F4}$$

For the spins governing both the feeding of SD and ND bands as well as the decay of the SD bands in ^{152}Dy, Eq. (F4) is assumed to be valid.

2. Cranking level density formulas

In Ref. [20], a level density formula appropriate for use with the cranking model is given as

$$\rho_I(U) = \frac{\sqrt{\pi}}{12} (aU)^{-1/4} U^{-1} e^{2\sqrt{a(U-\Delta)}}. \tag{F5}$$

In Refs. [23,33,71], the level density formula is proposed to be

$$\rho_I(U) = \frac{\sqrt{\pi}}{48} a^{-1/4} U^{-5/4} e^{2\sqrt{a(U-\Delta)}}, \tag{F6}$$

which is just 1/4 of the level density given in Eq. (F5). This factor originates from parity-signature selections. According to Ref. [23], the proper values of the level density parameter a in Eq. (F6) are $A/10$ and $A/17$ MeV^{-1} for the ^{152}Dy ND and SD wells, respectively.

[1] R. V. F. Janssens and T. L. Khoo, Annu. Rev. Nucl. Part. Sci. **41**, 321 (1991).

[2] P. J. Nolan, A. Kirwan, D. J. G. Love, A. H. Nelson, D. J. Unwin, and P. J. Twin, J. Phys. G **11**, L17 (1985).

[3] B. M. Nyako, J. R. Cresswell, P. D. Forsyth, D. Howe, P. J. Nolan, M. A. Riley, J. F. Sharpey-Schafer, J. Simpson, N. J. Ward, and P. J. Twin, Phys. Rev. Lett. **52**, 507 (1984).

[4] P. J. Twin, A. H. Nelson, B. M. Nyako, D. Howe, H. W. Cranmer-Gordon, D. Elenkov, P. D. Forsyth, J. K. Jabber, J. F. Sharpey-Schafer, J. Simpson *et al.*, Phys. Rev. Lett. **55**, 1380 (1985).

[5] P. J. Twin, B. M. Nyako, A. H. Nelson, J. Simpson, M. A. Bentley, H. W. Cranmer-Gordon, P. D. Forsyth, D. Howe, A. R. Mokhtar, J. D. Morrison *et al.*, Phys. Rev. Lett. **57**, 811 (1986).

[6] T. Lauritsen, M. P. Carpenter, T. Døssing, P. Fallon, B. Herskind, R. V. F. Janssens, D. G. Jenkins, T. L. Khoo, F. G. Kondev, A. Lopez-Martens *et al.*, Phys. Rev. Lett. **88**, 042501 (2002).

[7] T. Lauritsen, R. V. F. Janssens, M. P. Carpenter, P. Fallon, B. Herskind, D. G. Jenkins, T. L. Khoo, F. G. Kondev, A. Lopez-Martens, A. O. Macchiavelli *et al.*, Phys. Rev. Lett. **89**, 282501 (2002).

[8] I. Y. Lee, Nucl. Phys. **A520**, 641c (1990).

[9] T. Lauritsen, T. L. Khoo, I. Ahmad, M. P. Carpenter, R. V. F. Janssens, A. Korichi, A. Lopez-Martens, H. Amro, S. Berger, L. Calderin *et al.*, Phys. Rev. C **62**, 044316 (2000).

[10] R. G. Henry, T. Lauritsen, T. L. Khoo, I. Ahmad, M. P. Carpenter, B. Crowell, T. Døssing, R. V. F. Janssens, F. Hannachi, A. Korichi *et al.*, Phys. Rev. Lett. **73**, 777 (1994).

[11] R. Holzmann, T. L. Khoo, W. C. Ma, I. Ahmad, B. K. Dichter, H. Emling, R. V. F. Janssens, M. W. Drigert, U. Garg, M. A. Quader *et al.*, Phys. Rev. Lett. **62**, 520 (1989).

[12] R. Holzmann, I. Ahmad, B. K. Dichter, H. Emling, R. V. F. Janssens, T. L. Khoo, W. C. Ma, M. W. Drigert, U. Garg, D. C. Radford *et al.*, Phys. Lett. **B195**, 321 (1987).

[13] K. Schiffer, B. Herskind, and J. Gascon, Z. Phys. A **332**, 18 (1989).

[14] G. Leander, Phys. Rev. C **25**, 2780 (1982).

[15] B. Lauritzen, T. Døssing, and R. A. Broglia, Nucl. Phys. **A457**, 61 (1986).

[16] R. A. Broglia, T. Døssing, B. Lauritzen, and B. R. Mottelson, Phys. Rev. Lett. **58**, 326 (1987).

[17] F. S. Stephens, J. E. Draper, J. C. Bacelar, E. M. Beck, M. A. Deleplanque, and R. M. Diamond, Phys. Rev. C **37**, 2927 (1988).

[18] M. Matsuo, T. Døssing, B. Herskind, S. Frauendorf, E. Vigezzi, and R. A. Broglia, Nucl. Phys. **A557**, 211c (1993).

[19] S. Leoni, B. Herskind, T. Døssing, K. Yoshida, M. Matsuo, A. Atac, G. B. Hagemann, F. Ingebretsen, H. J. Jensen, R. M. Lieder *et al.*, Phys. Lett. **B353**, 179 (1995).

[20] T. Døssing, B. Herskind, S. Leoni, A. Bracco, R. A. Broglia, M. Matsuo, and E. Vigezzi, Phys. Rep. **268**, 1 (1996).

[21] A. Bracco, P. Bosetti, S. Frattini, E. Vigezzi, S. Leoni, T. Døssing, B. Herskind, and M. Matsuo, Phys. Rev. Lett. **76**, 4484 (1996).

[22] M. Matsuo, T. Døssing, E. Vigezzi, R. A. Broglia, and K. Yoshida, Nucl. Phys. **A617**, 1 (1997).

[23] K. Yoshida and M. Matsuo, Nucl. Phys. **A636**, 169 (1998).

[24] M. Matsuo, T. Døssing, E. Vigezzi, and R. A. Broglia, Phys. Lett. **B465**, 1 (1999).

[25] M. Matsuo, K. Yoshida, T. Døssing, E. Vigezzi, and R. A. Broglia, Nucl. Phys. **A649**, 379c (1999).

[26] S. Frattini, A. Bracco, S. Leoni, F. Camera, B. Million, N. Blasi, G. L. Bianco, M. Pignanelli, E. Vigezzi, B. Herskind *et al.*, Phys. Rev. Lett. **83**, 5234 (1999).

[27] T. Døssing, B. Herskind, A. Maj, M. Matsuo, E. Vigezzi, A. Bracco, S. Leoni, and R. A. Broglia, Acta Phys. Pol. B **32**, 2565 (2001).

[28] F. S. Stephens, M. A. Deleplanque, I. Y. Lee, D. Ward, P. Fallon, M. Cromaz, R. M. Clark, R. M. Diamond, A. O. Macchiavelli, and K. Vetter, Phys. Rev. Lett. **88**, 142501 (2002).

[29] S. Leoni, M. Matsuo, A. Bracco, G. Benzoni, N. Blasi, F. Camera, C. Grassi, B. Million, A. Paleni, M. Pignanelli *et al.*, Phys. Rev. Lett. **93**, 022501 (2004).

[30] S. Leoni, M. Matsuo, A. Bracco, G. Benzoni, N. Blasi, F. Camera, C. Grassi, B. Million, A. Paleni, M. Pignanelli *et al.*, AIP Conf. Proc. **764**, 309 (2005).

[31] M. A. Deleplanque, F. S. Stephens, I. Y. Lee, A. O. Macchiavelli, D. Ward, P. Fallon, M. Cromaz, R. M. Clark, M. Descovich, R. M. Diamond *et al.*, AIP Conf. Proc. **764**, 303 (2005).

[32] S. Åberg, Prog. Part. Nucl. Phys. **28**, 11 (1992).

[33] K. Yoshida and M. Matsuo, Nucl. Phys. **A612**, 26 (1997).

[34] M. Matsuo, S. Leoni, C. Grassi, E. Vigezzi, A. Bracco, Døssing, and B. Herskind, AIP Conf. Proc. **656**, 32 (2003).

[35] B. R. Mottelson, in *Proceedings of the International Seminar on the Frontier of Nuclear Spectroscopy* (World Scientific, Singapore, 1993).

[36] B. Lauritzen, R. A. Broglia, W. E. Ormand, and T. Døssing, Phys. Lett. **B207**, 238 (1988).

[37] B. R. Mottelson, Nucl. Phys. **A557**, 717c (1993).

[38] A. Lopez-Martens *et al.* (to be published).

[39] T. Døssing, A. P. Lopez-Martens, T. L. Khoo, and S. Åberg, AIP Conf. Proc. **764**, 27 (2005).

[40] O. Bohigas, M. J. Giannoni, and C. Schmit, Phys. Rev. Lett. **52**, 1 (1984).

[41] F. S. Stephens, M. A. Deleplanque, I. Y. Lee, A. O. Macchiavelli, D. Ward, P. Fallon, M. Cromaz, R. M. Clark, M. Descovich, R. M. Diamond *et al.*, Phys. Rev. Lett. **94**, 042501 (2005).

[42] M. A. Bentley, A. Alderson, G. C. Ball, H. W. Cranmer-Gordon, P. Fallon, B. Fant, P. D. Forsyth, B. Herskind, D. Howe, C. A. Kalfas *et al.*, J. Phys. G. **17**, 481 (1991).

[43] T. L. Khoo, R. K. Smither, B. Haas, O. Hausser, H. R. Andrews, D. Horn, and D. Ward, Phys. Rev. Lett. **41**, 1027 (1978).

[44] M. P. Carpenter, T. L. Khoo, I. Ahmad, R. V. F. Janssens, T. Lauritsen, G. A. Annan, A. M. Baxter, M. E. Bleich, S. Harfenist, E. F. Moore *et al.*, Nucl. Instrum. Methods. A **353**, 234 (1994).

[45] M. Hass, N. Benczer-Koller, G. Kumbartzki, T. Lauritsen, T. L. Khoo, I. Ahmad, M. P. Carpenter, R. V. F. Janssens, E. F. Moore, F. L. H. Woolfs *et al.*, Phys. Rev. C **44**, 1397 (1991).

[46] C. W. Beausang, D. Prevost, M. H. Bergstrom, G. deFrance, B. Haas, J. C. Lisle, C. Theisen, J. Timar, P. J. Twin, and J. N. Wilson, Nucl. Instrum. Methods. A **364**, 560 (1995).

[47] B. Crowell, M. P. Carpenter, R. G. Henry, R. V. F. Janssens, T. L. Khoo, T. Lauritsen, and D. Nisius, Nucl. Instrum. Methods. A **355**, 575 (1995).

[48] D. C. Radford, I. Ahmad, R. Holzmann, R. V. F. Janssens, and T. L. Khoo, Nucl. Instrum. Methods A **258**, 111 (1987).

[49] G. F. Knoll, *Radiation Detection and Measurement* (Wiley, New York, 2000).

[50] R. Holzmann, I. Ahmad, R. V. F. Janssens, T. L. Khoo, D. C. Radford, M. W. Drigert, and U. Garg, Nucl. Instrum. Methods. A **260**, 153 (1987).

[51] R. Firestone and V. Shirley, *Table of Isotopes* (Wiley, New York, 1996).

[52] T. K. Alexander and J. S. Forster, *Advances in Nuclear Physics* (Plenum, New York, 1968).

[53] R. M. Lieder and H. Ryde, Adv. Nucl. Phys. **10**, 1 (1978).

[54] S. J. Feenstra, Ph.D. thesis, Rijksuniversiteit Groningen, 1979.

[55] R. M. Diamond and F. S. Stephens, Annu. Rev. Nucl. Sci. **30**, 85 (1980).

[56] D. C. Radford, http://radware.phy.ornl.gov (2004).

[57] T. Yamazaki, Nucl. Data Sect. A **3**, 1 (1967).

[58] O. Andersen, J. D. Garrett, G. B. Hagemann, B. Herskind, D. L. Hillis, and L. L. Riedinger, Phys. Rev. Lett. **43**, 687 (1979).

[59] P. Benet, Ph.D. thesis, CRN Strasbourg, CRN/PN88-29, 1988.

[60] X-5 Monte Carlo Team, Los Alamos National Laboratory Report, LA-CP-03-0245, 2003 (unpublished).

[61] G. Audi, A. H. Wapstra, and C. Thibault, Nucl. Phys. **A729**, 337 (2003).

[62] T. Lauritsen, P. Benet, T. L. Khoo, K. B. Beard, I. Ahmad, M. P. Carpenter, P. J. Daly, M. W. Drigert, U. Garg, P. B. Fernandez *et al.*, Phys. Rev. Lett. **69**, 2479 (1992).

[63] E. Vigezzi, R. A. Broglia, and T. Døssing, Nucl. Phys. **A520**, 179c (1990).

[64] E. Vigezzi, R. A. Broglia, and T. Døssing, Phys. Lett. **B249**, 163 (1990).

[65] H. A. Weidenmüller, P. von Brentano, and B. R. Barrett, Phys. Rev. Lett. **81**, 3603 (1998).

[66] J. Gu and H. A. Weidenmüller, Nucl. Phys. **A660**, 197 (1999).

[67] D. M. Cardamone, C. A. Stafford, and B. R. Barrett, Phys. Rev. Lett. **91**, 102502 (2003).

[68] C. A. Stafford and B. R. Barrett, Phys. Rev. C **60**, 051305(R) (1999).

[69] A. J. Larebee *et al.* (to be published).

[70] T. R. Werner and J. Dudek, Phys. Rev. C **44**, R948 (1991).

[71] K. Yoshida, M. Matsuo, and Y. R. Shimizu, Nucl. Phys. **A696**, 85 (2001).

[72] A. Bohr and B. R. Mottelson, *Nuclear Structure,* Vol. 1 (Benjamin, New York, 1969).

[73] G. A. Leander, Comput. Phys. Commun. **47**, 311 (1987).

[74] A. Bohr and B. R. Mottelson, *Nuclear Structure* Vol. 2 (Benjamin, New York, 1969).

[75] S. Åberg, Nucl. Phys. **A477**, 18 (1988).

[76] J. Dudek, B. Herskind, W. Nazarewicz, Z. Szymanski, and T. R. Werner, Phys. Rev. C **38**, 940 (1988).

[77] S. Henss, A. Ruckelshausen, R. D. Fischer, W. Kuhn, V. Metag, R. Novotny, R. V. F. Janssens, T. L. Khoo, D. Habs, D. Schwalm *et al.*, Phys. Rev. Lett. **60**, 11 (1988).

[78] P. Ring and P. Schuck, *The Nuclear Many-Body Problem* (Springer-Verlag, New York, 1980).

[79] P. Axel, Phys. Rev. **126**, 671 (1962).

[80] G. A. Bartholomew, E. D. Earle, A. J. Ferguson, J. W. Knowles, and M. A. Lone, Adv. Nucl. Phys. **7**, 229 (1973).

[81] G. A. Bartholomew, Annu. Rev. Nucl. Sci. **11**, 259 (1961).

[82] L. P. Farris, J. A. Cizewski, M. J. Brinkman, R. G. Henry, C. S. Lee, T. L. Khoo, R. V. F. Janssens, M. P. Carpenter, I. Ahmad, T. Lauritsen *et al.*, in Proceedings, International Conference on Nuclear Structure at High Angular Momentum, Ottowa, 1992 May 18–21, AECL 10613 (1992), p. 71.

[83] L. P. Farris, Ph.D. thesis, Rutgers University, 1993.

[84] J. S. Levinger and H. A. Bethe, Phys. Rev. **78**, 115 (1950).

[85] S. G. Kadmemskii, V. P. Markushev, and V. I. Furman, Sov. J. Nucl. Phys. **37**, 165 (1983).

[86] G. A. Leander, Phys. Rev. C **38**, 728 (1988).

[87] H. Ejiri and M. J. A. de Voight, *Gamma-Ray and Electron Spectroscopy in Nuclear Physics* (Clarendon, Oxford, 1989).

[88] B. Bush and Y. Alhassid, Nucl. Phys. **A531**, 27 (1991).

[89] K. A. Snover, Annu. Rev. Nucl. Sci. **36**, 545 (1986).

[90] D. L. Hill and J. A. Wheeler, Phys. Rev. **89**, 1102 (1953).

[91] S. Bjørnholm and J. E. Lynn, Rev. Mod. Phys. **52**, 725 (1980).

[92] G. A. Lalazissis and P. Ring, Phys. Lett. **B427**, 225 (1998).

[93] P. J. Dagnall, C. W. Beausang, P. J. Twin, M. A. Bentley, F. A. Beck, T. Byrski, S. Clarke, D. Curien, G. Duchene, G. de France *et al.*, Phys. Lett. **B335**, 313 (1994).

[94] J. M. Blatt and V. F. Weisskopf, *Theoretical Nuclear Physics* (Wiley, New York, 1952).

[95] T. Lauritsen, R. V. F. Janssens, T. L. Khoo, I. Ahmad, M. P. Carpenter, F. G. Kondev, C. J. Lister, E. F. Moore, D. Seweryniak, S. Zhu *et al.*, AIP Conf. Proc. **819**, 459 (2006).

[96] D. Nisius, R. V. F. Janssens, E. F. Moore, P. Fallon, B. Crowell, T. Lauritsen, G. Hackman, I. Ahmad, H. Amro, S. Asztalos *et al.*, Phys. Lett. **B392**, 18 (1997).

[97] R. Bass, Nucl. Phys. **A231**, 45 (1974).

[98] S. Cohen, F. Plasil, and W. J. Swiatecki, Ann. Phys. (NY) **82**, 557 (1974).

[99] J. P. Vivien, D. Balouka, B. Haas, H. R. Andrews, D. C. Radford, D. Ward, V. P. Janzen, D. Prevost, J. C. Waddington, S. Flibotte *et al.*, Phys. Lett. **B278**, 407 (1992).

[100] K. Lagergren *et al.* (to be published).

[101] A. O. Macchiavelli (private communication).

[102] K. Siegbahn, *Alpha-, Beta- and Gamma-ray Spectroscopy* (North-Holland, Amsterdam, 1965).

[103] T. Døssing and A. S. Jensen, Nucl. Phys. **A222**, 493 (1974).